Stockholm University

# A search for Dark Matter Annihilations in the Sun with IceCube and Related Studies

Licentiate thesis

Matthias Danninger
Stockholm University, Department of Physics

Akademisk avhandling för avläggande av
filosofie licentiatexamen vid Stockholms universitet

August, 2011

Stockholm University
Department of Physics
http://www.fysik.su.se/

Stockholm
University

Matthias Danninger:
danning@fysik.su.se
**Supervisors:**
Prof. Klas Hultqvist
Prof. Per Olof Hulth
Docent Christian Walck

*Front page figure:* Emperor penguin wondering about Dark Matter

## Abstract

Dark matter could be indirectly detected through the observation of neutrinos produced as part of its self-annihilation process. Possible signatures are an excess neutrino flux from the Sun, where dark matter could be gravitationally trapped. The recent commissioning of the full DeepCore sub-array, a low-energy extension of the IceCube neutrino observatory, offers exciting opportunities for neutrino physics in the energy region of 10 GeV to 1 TeV. DeepCore's improved energy reach will, in particular, provide sensitivity to neutrinos from attractive WIMP candidates, like the neutralino or the lightest Kaluza-Klein particle (LKP), down to WIMP masses in the region of about 50 GeV. This will lead to stringent upper limits on the flux of muons from dark matter annihilations in the Sun and constraints on WIMP-proton cross-sections. This thesis reports on the search for dark matter annihilations in the Sun with the IceCube neutrino detector in the originally planned 86-string configuration, which includes the full DeepCore sub-array. The expected sensitivity for the detector livetime of 180 days is calculated for the Neutralino and the LKP for the IceCube detector with and without the DeepCore sub-array. This allows a detailed estimation of the expected benefit for low mass WIMP searches with DeepCore.

This thesis has four papers attached. Paper I and II discuss the extension of the conventional solar Dark Matter searches with IceCube to include the search for the LKP. Paper III describes an analysis of the IceCube-79 string configuration data to search for neutrinos that might be emitted along with the observed X-rays and $\gamma$-rays of the unusual September 2010 flare state of the Crab Nebula. The fourth paper reports on the current status of the IceCube-79 string solar WIMP analysis.

# Contents

**1 Introduction** **1**
1.1 About this thesis . . . . . 2
1.2 Author's contribution . . . . . 3
1.3 Acknowledgments . . . . . 5

**I Theoretical Overview** **7**

**2 Dark Matter** **9**
2.1 Energy and Matter Densities in the Universe . . . . . 9
2.2 Dark Matter Problem . . . . . 10
2.3 Dark Matter Candidates . . . . . 11
2.4 Relic Density of WIMPs . . . . . 12
2.5 The MSSM and the Neutralino . . . . . 13
2.6 Extra Dimensions and Kaluza-Klein-DM . . . . . 15
2.7 Current Experimental status of Dark Matter searches . . . . . 19
2.8 Indirect Solar Search for WIMP Dark Matter . . . . . 22

**3 High energy neutrino detection** **29**
3.1 Neutrino-nucleon interactions . . . . . 29
3.2 Muons in ice . . . . . 32
3.3 Cherenkov radiation . . . . . 33
3.4 Propagation of light in the South Pole ice . . . . . 34

**4 Background sources** **36**
4.1 Atmospheric muons . . . . . 36
4.2 Atmospheric neutrinos . . . . . 37
4.3 Neutrinos from the solar atmosphere . . . . . 37
4.4 Galactic neutrinos . . . . . 39
4.5 Cosmological neutrinos . . . . . 40

**II Experimental Overview 41**

**5 IceCube neutrino observatory 43**
5.1 IceCube . . . 44
5.2 sub-detectors . . . 46
5.3 IceCube digital optical module . . . 47
5.4 Data acquisition . . . 49
5.5 Trigger algorithm in IceCube-79 . . . 49
5.6 Trigger development studies . . . 50
5.6.1 Cylinder trigger . . . 50
5.6.2 Track engine trigger . . . 51
5.7 Data Filtering and processing . . . 58

**6 IceCube-80 + DeepCore-6 solar WIMP sensitivity 59**
6.1 Introduction and conventions . . . 59
6.2 Analysis cut levels . . . 65
6.3 Sensitivity . . . 73
6.4 Discussion . . . 75

# Chapter 1

# Introduction

Understanding our Universe and its evolution throughout the past billion years since the Big Bang is one of the major quests of modern physics and astronomy. This means in particular, to understand what our Universe is made of. The currently most accurate observations and measurements of the various matter and energy densities in the Universe suggest a total matter content of approximately 28%. Of this total matter content only 17% can be identified with common matter e.g., photons, atoms and neutrinos. The remaining 83% is of unknown origin and does not interact with ordinary matter through electromagnetic interaction and hence, is unseen dark matter.

While the presence of dark matter in the Universe has been inferred through its gravitational interactions, it has yet to be directly or indirectly observed. One of the most promising and experimentally accessible candidates for dark matter are so-called Weakly Interacting Massive Particles (WIMPs). In current models, WIMPs are predicted to have a mass in the range of a few tens of GeV to a few TeV. Whatever their underlying physics, these WIMPs may be swept up by the Sun on its transit through the galactic halo and become gravitationally bound by scattering weakly on solar nucleons. Over time, this leads to an accumulation of dark matter in the center of the Sun, exceeding the mean galactic density. Self-annihilation to standard model particles may result in a flux of high energy neutrinos that will be spectrally dependent on the annihilation channel and WIMP mass, and which can be searched for as a point-like source with neutrino telescopes such as IceCube.

A neutrino traveling through the Earth will occasionally interact within the Antarctic ice or surrounding bedrock, resulting in the creation of a daughter

lepton. In the case of an electron, the energy will be quickly dispersed in an electromagnetic cascade. A muon, on the other hand, can travel for several kilometers, depending on the medium. High energy muons emit Cherenkov radiation as they travel that can be detected if the medium is optically transparent, such as the deep clear ice at the South Pole. By recording the arrival times and intensities of these photons using optical sensors, the direction and energy of the muon and parent neutrino may be reconstructed.

The IceCube Neutrino Telescope instruments 1 $km^3$ of glacial ice at the South Pole with 5160 Digital Optical Modules (DOMs) on 86 strings deployed between depths of 1450m and 2450m. Each DOM consists of a 25 cm photomultiplier tube (PMT) and associated electronics enclosed in a glass pressure sphere. Eight more densely instrumented strings optimized for low energies plus the 12 adjacent standard strings at the center of the detector geometry make up the DeepCore subarray, which increases the sensitivity at low energies and substantially lowers the energy threshold. In addition, by using the surrounding IceCube strings as a veto, DeepCore will enable searches at low energies in the southern hemisphere, transforming IceCube into a full sky observatory.

## 1.1 About this thesis

This thesis is roughly divided into two main parts. Part I gives an introduction to the Dark Matter problem in the universe, proposed solutions and a discussion of past and current experimental efforts undertaken to discover Dark Matter with focus on indirect detection for dark matter annihilation signals from the Sun in neutrino telescopes (chapter 2). The first part continues with principles of neutrino detection (chapter 3) and ends with a detailed discussion about potential background sources for an indirect solar search for WIMP Dark Matter (chapter 4). Part II, the experimental part, starts with a detailed description of the IceCube neutrino observatory and the various steps within the data acquisition system with a focus on low energy trigger development studies (chapter 5). In chapter 6, I describe a solar WIMP sensitivity study for the full 86 string detector, using the initially proposed DeepCore geometry consisting of 6 additional strings.

The attached papers are:

Paper **I**: Danninger, Matthias and Han, Kahae for the IceCube Collaboration, *Search for the Kaluza-Klein Dark Matter with the AMANDA/IceCube Detectors*, *Proc. of the 31st. ICRC, arXiv:0906.3969v1* [astro-ph.HE], June, 2009.

Paper **II**: Abbasi, R. and others, *Limits on a muon flux from Kaluza-Klein dark matter annihilations in the Sun from the IceCube 22-string detector*, *Phys. Rev. D.* 81. 057101, 2010

Paper **III**: Abbasi, R. and others, *Neutrino analysis of the September 2010 Crab Nebula flare and time-independent constraints on neutrino emission from the Crab using IceCube*, *submitted to Astropart. Phys.*, May, 2011.

Paper **IV**: Danninger, Matthias and Strahler, Erik for the IceCube Collaboration, *Searches for Dark Matter Annihilations in the Sun with IceCube and DeepCore in the* 79*-string configuration*, *Proc. of the 32nd. ICRC*, June, 2011.

The first paper is a result from a continuation of my Diploma work, describing a data analysis for the Search for Kaluza-Klein dark matter with the combined AMANDA and IceCube-22 string detectors. Paper II is based on the search in Ref. [1], where we extended the existing IceCube-22 string analysis to limits on Kaluza-Klein dark matter. Paper III is a direct application of the sensitivity study, described in chapter 6, and an excellent check of the current quality and readiness of the analysis chain. Because of the unusual flare state of the Crab Nebula, IceCube initiated a fast analysis of the 79 string configuration data to search for neutrinos that might be emitted along with the observed X-rays and $\gamma$-rays. Two different data selections were performed, where one of them was a selection based on the solar WIMP analysis, discussed here. The fourth paper is a second ICRC contribution, describing the current status of the IceCube-79 string solar WIMP analysis.

## 1.2 Author's contribution

The work as a Ph.D student at Stockholm University during the first 2 $\frac{1}{2}$ years, that is described within this licentiate thesis, was carried out within

the IceCube Collaboration. This Collaboration consists of many skillful scientists, and therefore each personal contribution should always be regarded as part of a team effort within IceCube. My contributions have been the following:

- Preparing and executing final acceptance tests, FATs, for IceCube digital optical modules, DOMs, at Uppsala University.
- Lead of the DOM testing team during the last deployment season 2010/2011 carrying out the so-called South Pole FATs. Additionally, I helped as part of the deployment team, deploying IceCube strings and IceTop tanks.
- I accompanied an IceTop tank in a container from Sweden to South America as well as from Mc.Murdo station to South America on the Swedish icebreaker Oden in order to perform a latitude scan of the cosmic muon flux. I took part in this mission to oversee data acquisition and storage, and also helped during the set-up and freezing process of the IceTop tank in Uppsala.
- Sensitivity study for a solar WIMP search with the IceCube-86 string detector including DeepCore (paper IV)
- Contributed with event selection to the IceCube-79 string data analysis of the September 2010 Crab Nebula flare (paper III)
- Extended for a first time solar WIMP searches with the IceCube and AMANDA detectors to alternative dark matter candidates (paper I + II)
- Intensive low energy trigger studies, including Volume Trigger (now Cylinder Trigger) and Track Engine studies and developments and their implementation into the IceCube software
- On-line trigger and filter studies, improvements and implementations for the 79-string season as well as the 86-string season

Additionally, I represented the IceCube Collaboration with a talk at the 2010 Penn. State low-energy Neutrino workshop, 'Prospects for Dark Matter Searches with DeepCore', a talk at the Ohio State Novel Searches for Dark Matter workshop 2010 'IceCube/DeepCore overview and DM searches' and a talk at TeVPA 2010 in Paris 'Searches for Dark Matter Annihilations in the Sun and Earth with IceCube and DeepCore'.

## 1.3 Acknowledgments

First of all, I want to thank my supervisors Prof. Klas Hultqvist, Dr. Christian Walck and Prof. Per Olof Hulth for many technical discussions, guidance and helping me to find the right path within my various projects. Especially, I want to thank here again Prof. Per Olof Hulth, for supporting me to be able to undertake the long sea journey with the icebreaker Oden and gifting me various talks at conferences and workshops. Thanks a lot of course to the whole Stockholm IceCube group and also the Uppsala IceCube group (here also special thanks to Prof. Allan Hallgren for the Oden project support).

# Part I

# Theoretical Overview

# Chapter 2

# Dark Matter

## 2.1 Energy and Matter Densities in the Universe

The dark matter problem in the Universe can be deduced from past and present astronomical and physical observations, and how these influence cosmological models. General relativity, the remarkably successful underlying theory of cosmology, describes in the form of Einstein's equations the relation between the curvature of spacetime, the geometry of the Universe, and its energy and mass content. Einstein originally introduced the cosmological constant, $\Lambda$, to get a non-expanding solution, a so-called stationary Universe. More recently, after the discovery of an accelerating expansion of the Universe through type Ia supernova observations [2], $\Lambda$ is linked with an extra repulsive force, called 'vacuum' or 'dark' energy, which contributes as a source of gravitation fields even in the absence of matter [3]. Dark energy is also of unknown origin, but will not be discussed in detail here. Although, there exist other not yet excluded models that do not resort to dark energy [4, 5], rather take into account the observer's own special position within our lumpy universe in order to interpret cosmological distance and time measurements differently, the so-called concordance model of cosmology is considered the underlying theory of cosmology throughout the thesis.

Measurements of the Cosmic Microwave Background (CMB) [6] show that the Universe is isotropic and homogeneous on large scales. A metric can be defined, describing the observed symmetries, and expressed in the Robertson-

Walker form, in order to make predictions for average mass densities,

$$ds^2 = -dt^2 + a^2(t)\left[\frac{dr^2}{1-kr^2} + r^2 d\Omega^2\right] \quad , \quad k = -1, 0, 1 \tag{2.1}$$

with the scale factor $a(t)$. Choosing the constant $k$, denoting the spatial curvature, to be zero, an expression for the critical energy density, $\rho_c$, in a flat Universe can be derived [7]

$$\rho_c = \frac{3H^2}{8\pi G_N} \ , \tag{2.2}$$

where the expansion rate of the Universe, $H$, is the Hubble parameter and $G_N$ is Newton's constant. This allows any energy or matter density, $\Omega_i = \rho_i/\rho_c$, contributing to the total energy density of the Universe, $\Omega = \sum_i \Omega_i$, to be expressed in terms of $\rho_c$.

## 2.2 Dark Matter Problem

The first indication of large quantities of 'unseen' or dark mass was noted by Fritz Zwicky after studies of the Coma galaxy cluster as early as 1933 [8]. He observed that the orbital velocity, $v$, of objects outside the central region did not follow the expected spectrum derived from Kepler's third law and the visible matter distribution. But it was not until Vera Rubin [9] in 1970 studied rotation curves of galaxies that the so-called *galaxy rotation problem* became more apparent. Taking into account only luminous matter, the orbital velocity of stars as a function of their distance from the galaxy center should be proportional to $1/\sqrt{r}$ beyond the optical disk. The observed rotation curves have a characteristic flat behavior beyond the optical disk, which is equivalent to a constant orbital velocity, and implies the existence of a halo with a mass distribution, $M(r)$, following $M(r) \propto r$ and $\rho \propto 1/r^2$.

An alternative approach to describe the *galaxy rotation problem* are the so-called modified Newtonian dynamics theories, MOND. Instead of explaining the observation with a new kind of matter, Newton's laws of gravity are modified at large distances [10]. These theories however, fail to explain all observations, if applied on their own, and are therefore disfavored [11]. Another demonstrative experimental piece of evidence for DM on larger scales than galaxies, is weak and strong gravitational lensing of distant stars or galaxies on passing foreground galaxy clusters [12]. There exists further observational evidence, but the striking point is that all these observations are

based on various independent physical principles and yet all lead to the same conclusion, an additional non baryonic matter component.

The currently most accurate determinations of the various matter and energy densities $\Omega_i$ come from global fits of cosmological parameters to a variety of observations, e.g. the measurements of the CMB anisotropy. Following the notation introduced in section 2.1, the total energy density in the Universe derived from the combined results of WMAP and SDSS LRG [13] is $\Omega = 1.003^{+0.010}_{-0.009}$. This indicates a close to spatially flat Universe with a dark energy content of $\Omega_\Lambda = 0.761^{+0.017}_{-0.018}$ and a total matter density of $\Omega_m = 0.239^{+0.018}_{-0.018}$. The dark matter density is found to be $\Omega_{DM} = 0.197^{+0.016}_{-0.015}$ and is therefore almost five times larger than the density of ordinary matter, also referred to as baryonic matter $\Omega_b = 0.0416^{+0.019}_{-0.018}$ [13].

## 2.3 Dark Matter Candidates

The most intuitive candidates for dark matter are massive compact halo objects (MACHOS) or clouds of non-luminous interstellar gas, consisting of ordinary matter. Weak gravitational micro lensing of stars in the Magellanic Clouds by the gravitational fields of MACHOs in-between, provides evidence of such form. But, strict limits on the baryonic density in the Universe are set by the theory of Big Bang nucleo-synthesis [14]. Therefore, compact objects like MACHOs or non-illuminated gas clouds can only make up a very small fraction of dark matter. Consequently, the observational evidence listed in section 2.2 cannot be explained by ordinary matter. Although Standard Model neutrinos undoubtedly contribute to dark matter, they are no longer favored as a dominant dark matter component. Neutrinos have extremely small masses and calculations of the total neutrino relic density show that neutrinos are simply not abundant enough and their maximal contribution to the total energy density ($\Omega_\nu < 0.024$ at 95% confidence level) is less than $\Omega_b$ [13].

The Standard Model (SM) of particle physics cannot provide a viable dark matter candidate. As a consequence, a whole zoo of possible dark matter particles have been introduced in models beyond the SM. They can be divided into hot, warm and cold dark matter, according to the speed of the particles at decoupling. CMB measurements [13] and structure formation of the Universe, studied in numerical N-Body simulations, favor non-relativistic, i.e., cold particles, removing relativistic (hot) and semi-relativistic (warm) dark matter as preferred candidates [15]. The most promising dark matter can-

didates are Weakly Interacting Massive Particles (WIMPs), which carry no electrical charge and interact only weakly and gravitationally with matter. As products of the hot Big Bang, WIMPs require a lifetime longer than the current age of the Universe and the maximum energy must not exceed the over-closure limit of the order of 10 TeV. Constraints at the lower end of the energy spectrum are set by the most recent collider experiments [16]. This thesis will focus on the most widely studied WIMP candidates, the neutralino, $\chi$, as introduced by the Minimal Supersymetric extension of the Standard Model (MSSM) (see section 2.5) and the Lightest Kaluza-Klein Particle (LKP), introduced in section 2.6, which is predicted by theories of Universal Extra Dimensions (UED) (see section 2.6).

## 2.4 Relic Density of WIMPs

Calculations of particle dynamics in the early universe can determine whether the predicted WIMPs have a high enough relic abundance in the present universe. Assuming the existence of theoretically motivated WIMPs, their relic density has to agree with the observed DM density $\Omega_{\mathrm{DM}} = 0.197^{+0.016}_{-0.015}$. The present relic density of a WIMP, motivated by one of the above mentioned theories, can be calculated, if the WIMPs were in thermal and chemical equilibrium during the primordial nucleosynthesis after the period of inflation. Following the calculations of [7], the Boltzmann equation for the particle number density $n_x$ of the WIMP of type $x$ is given by,

$$\frac{dn_x}{dt} + 3Hn_x = -\langle\sigma v\rangle \left(n_x^2 - (n_x^{\mathrm{eq}})^2\right) \tag{2.3}$$

with $\langle\sigma v\rangle$ being the thermally averaged total annihilation cross section multiplied by the relative velocity. The number density, $n_x^{\mathrm{eq}}$, at thermal equilibrium for a temperature, $T$, is given in the non-relativistic limit for massive WIMPs with mass $m_x$, using the Maxwell-Boltzmann approximation

$$n_x^{\mathrm{eq}} = g_x \left(\frac{m_x T}{2\pi}\right)^{3/2} e^{-m_x/T} \ , \tag{2.4}$$

where $g_x$ is the number of internal degrees of freedom of the WIMP. At temperatures of $T \sim 10^1 - 10^3$ GeV, when the WIMPs are beginning to no longer be in thermal equilibrium with the expanding Universe, equation 2.3 is dominated by the expansion rate, $H$, and annihilation processes into lighter SM particles are beginning to exceed the number of WIMP creations. After the interaction rate, $\Gamma$, of the WIMP drops below $H$, annihilation

processes freeze out completely. After freezout, the conservation of entropy per comoving volume, $sa^3$, allows one to approximate the matter density of WIMPs,

$$\Omega_x h^2 \approx const. \cdot \frac{T_0^3}{M_{\mathrm{Pl}}^3 \langle \sigma v \rangle} \approx \frac{0.1\mathrm{pb} \cdot c}{\langle \sigma v \rangle} \tag{2.5}$$

Here $T_0$ is the current CMB temperature, $M_{Pl}$ the Planck mass and c the speed of light. Given the current best measurement of $\Omega_{DM}$, it is most intriguing that in eq. 2.5, the interaction cross section turns out to be near the typical size of weak scale interactions. The calculation holds for theoretically motivated WIMPs in general and is a strong argument for WIMPs being dark matter. This rather astonishing theoretical match between DM and WIMPs is often referred to as the 'WIMP miracle'.

The above calculation of the relic WIMP density assumes only one particle, the lightest particle that is protected against decay by some symmetry, i.e. R-parity or KK-parity, for neutralinos or KK particles, respectively, to accredit for the final CDM density. This is a good first approximation, but inaccurate. This is especially relevant for the case of particles that share a quantum number and have masses only slightly heavier then the relic particle. These particles have an abundance very similar to $n_x^{\mathrm{eq}}(T)$ in the hot Big Bang, and their freeze out temperatures are of the same order. Therefore, the calculation of the relic density has to be extended to also account for coannihilations [3, 7]. Any relic abundance of higher order will eventually decay into the stable ground state of the relic WIMP and contribute towards the total relic abundance $n_x = \sum_{i=0}^{N} n_i$, where $n_i$ is the number density of a relic particle $i$ with mass $m_i > m_x$.

## 2.5 The MSSM and the Neutralino

The SM of particle physics has a fundamental distinction between fermions, half-integer spin particles, and bosons, integer spin particles. Fermions are the constituents of matter, while bosons are the force carriers of interactions. Within the SM, there exists no symmetry to relate the nature of forces and matter. The framework of supersymmetry, SUSY, provides a unified picture between matter and interactions [17]. Additionally, SUSY provides a possible solution to the so-called hierarchy problem, which is linked to the enormous difference between the electroweak and Planck energy scales. Within this thesis, the minimal supersymmetric standard model, the MSSM, is considered. It is minimal in a sense that it has the smallest possible field content neces-

sary to give rise to all SM fields [3]. This introduces a fermionic superpartner for each SM gauge boson. Gluons $g$, mediators of the strong force, and $W^{\pm}$ and $B$ bosons, mediators of the electroweak force, get partners called gluinos $\tilde{g}$, winos $\tilde{W}$ and binos $\tilde{B}$, respectively. All SM fermions, quarks ($q$) and charged leptons ($l$), get scalar superpartners called squarks ($\tilde{q}$) and sleptons ($\tilde{l}$), whereas neutrinos ($\nu$) become sneutrinos ($\tilde{\nu}$). The neutral Higgs triplet, $H_1^0$, $H_2^0$ and the longitudinal spin state of the Z, $H_3^0$, get two superpartners, $\tilde{H}_1^0$ and $\tilde{H}_2^0$. The MSSM introduces a new multiplicative quantum number,

$$R \equiv (-1)^{3B+L+2s} \ , \tag{2.6}$$

called R-parity, where $B$ is the baryon number, $L$ the lepton number and $s$ the spin of the particle or superparticle (sparticles). SM particles have R-parity $R = 1$, while all sparticles have R-parity $R = -1$. As a consequence of R-parity conservation, sparticles can only decay into an odd number of lighter sparticles plus SM particles. Therefore, R-parity conservation results in a lightest supersymmetric particle, the LSP, which makes an excellent DM candidate.

## The lightest neutralino

At first impression, it might seem that many Sparticles are suitable candidates for being the LSP. Observational constraints limit the LSP to be neutral, thus carry no electrical charge or color. Therefore, within the MSSM, the LSP is either the lightest Sneutrino or the lightest neutralino. Sneutrinos as LSPs have been excluded by direct DM detection experiments [18], leaving the lightest neutralino as the most widely studied candidate for the LSP and hence, as DM candidate. As mentioned above, the superpartners of the photon and $Z$ boson and the neutral Higgs bosons, $H_1^0$ and $H_2^0$, are $\tilde{B}$, $\tilde{W}$, $\tilde{H}_1^0$ and $\tilde{H}_2^0$. These Sparticles mix into four Majorana fermionic mass eigenstates that are named neutralinos and labeled in the order of increasing mass as $\tilde{\chi}_1^0$, $\tilde{\chi}_2^0$, $\tilde{\chi}_3^0$ and $\tilde{\chi}_4^0$. The notation for the lightest neutralino,

$$\chi \equiv \tilde{\chi}_1^0 = n_{11}\tilde{B} + n_{12}\tilde{W}_3 + n_{13}\tilde{H}_1^0 + n_{14}\tilde{H}_2^0 \ , \tag{2.7}$$

is a linear combination of gauginos and higgsinos which will simply be referred to as $\chi$, throughout the thesis. The linear coefficients from eq. 2.7 can be summarized in the gaugino fraction, $f_G = n_{11} + n_{12}$, and the higgsino fraction, $f_H = n_{13} + n_{14}$. How much 'gaugino-like' or 'higgsino-like' is the $\chi$, or in other words, what determines the characteristics of the $\chi$? The exact identity of the $\chi$ depends on the given supersymmetric scenario. If the MSSM would

not be broken, all spartners would have the same mass as the corresponding SM particles. This is not observed in Nature, and therefore supersymmetry breaking terms are added to the theory. The MSSM, although it is called 'minimal', has as many as 124 free parameters. In order to be able to make practical phenomenological studies of the MSSM, additional assumptions are added to limit the number of free parameters. Among the most widely studied scenarios are the constrained MSSM, cMSSM, and the MSSM-7, which is modeled e.g. within DarkSusy [19] and uses only a 7 parameter subset. Each model results in a characteristic neutralino, with specific mass, cross sections and branching ratios. The cross section of the $\chi$ is at the weak scale and its mass is limited by accelerator based measurements at the lower end of the spectrum to $m_\chi > 46$ GeV, while the overclosure limit gives the upper bound $m_\chi <\sim 10$ TeV. Respecting R-parity conservation, the $\chi$ can pair-annihilate due to its Majorana character into many possible SM particles:

$$\chi\chi \rightarrow \begin{cases} l\bar{l}, q\bar{q}, W^+W^-, Z^0Z^0, gg, \gamma\gamma, \\ H_1^0H_3^0, H_2^0H_3^0, \\ Z^0H_1^0, Z^0H_2^0, W^+H^-, W^-H^+, Z^0\gamma \end{cases} \tag{2.8}$$

Under the assumption of the $\chi$ being CDM, it is non-relativistic with low velocities of $\sim 220$ km/s. At these velocities, the leading annihilation channel is into heavy fermion-antifermion pairs, like top, bottom and charm quarks and tau leptons, as well as heavy gauge boson pairs, like $W^+W^-$ and $Z^0Z^0$ pairs. Annihilation channels into final states including Higgs bosons are also favored over channels into light fermion-antifermion pairs that are helicity suppressed in the relativistic limit that is easily reached for light final states (e.g. direct $\nu\bar{\nu}$ channel). The direct photon channel can only occur at the 'loop'-level, as $\chi$ is electrically neutral and thus does not couple to photons.

## 2.6 Extra Dimensions and Kaluza-Klein-DM

Our every-day world appears to consist of three space dimensions and one time dimension, the $3 + 1$ space-time. The first attempts to extend this dimensionality were made by Kaluza [20] and Klein [21], proposing that a unification of electrodynamics and gravitation might be achievable in a single five dimensional gravitational theory. Based on that concept, various models have been suggested, with possible extra dimensions appearing at higher energy scales.

## Concept of Universal Extra Dimensions

In the framework of extra dimensions, the ordinary 3+1 space-time is referred to as the brane, which is embedded in a higher-dimensional $3 + \delta + 1$ space-time called the bulk. There are strong phenomenological motivations, like dynamical electroweak symmetry breaking (EWSB) [22], to have all gauge fields propagating in the bulk. This scenario, with compactified, spatially flat, extra dimensions is called the Universal Extra Dimensions (UED) scenario. The additional compactified dimensions are finite and have periodic boundary conditions. It is shown in Ref. [22] that, in the case of one extra dimension, the constraint on the compactification scale is given by $R^{-1} > 300$ GeV, where $R$ is the compactification radius. The main motivation for using the theory of UED in this thesis is the prediction of the LKP as a potential WIMP candidate (section 2.6). UED has a relatively small number of free parameters to describe the introduced WIMP, compared to the MSSM. The most essential parameter is the mass, given by the inverse of the compactification scale $R$ at tree level.

## Kaluza-Klein Dark Matter

An example of a class of particles arising from compactified dimensions are 'pyrgons' [23]. Pyrgon is the Greek word for ladder or tower, which characterizes the particles, in general called KK-particles. Assuming there are KK excitations of SM particles, it is shown in the following that the expected spectrum of particles yields viable DM candidates. A simple example is the case of one circular extra dimension with radius $R$ where a massless quantum field $A(x)$, propagating in the circular extra dimension, defined by $R$, can also be regarded as a 4-dimensional field with a tower of mass eigenstates $m_n = n/R$ at tree level. More precisely, $A(x)$ depends on $x = (\mathbf{x}, \mathbf{y})$, where $\mathbf{x} = (x_0, x_1, x_2, x_3)$ is the normal 4-dimensional space-time and $\mathbf{y}$ is the extra dimensional coordinate. Due to the circular shape of the extra dimension, the periodic boundary condition for the $\mathbf{y}$-coordinate can be expressed as invariance under the transformation $\mathbf{y} \to \mathbf{y} + 2\pi R$. Consequently, the field $A(x)$ appears in a set of Fourier expanded modes, which are called KK-states,

$$A(x) = \sum_{n=-\infty}^{\infty} A^{(n)}(\mathbf{x}) e^{(\frac{i\ n\ \mathbf{y}}{R})} \quad \text{with} \quad n \in Z; \tag{2.9}$$

The 4-dimensional fields $A^{(n)}(\mathbf{x})$ are the corresponding KK-modes with $n$ being the KK-excitation number. The zero-mode field $A^{(0)}(\mathbf{x})$ corresponds

to the usual 4-dimensional state of the SM particles. The extra dimension affects possible observation by an appearance of the same SM particle with different masses, associated with KK-states of increasing mass [24].

The exponential term in equation 2.9 can be identified with a $U(1)$ symmetry in the brane. Thus, the momentum $p \equiv n/R$ is quantised in the extra dimension and $n$ becomes a good quantum number, the KK-number [25]. This can be also expressed in terms of UED, where the first excitation of KK-particles is,

$$m_{KK}^2 = \frac{1}{R^2} + m_{SM}^2 \tag{2.10}$$

with the mass of the zero-level KK-mode of the SM particle $m_{SM}$. This indicates a high degree of degeneracy for light SM particles at tree level. However, corrections at the one-loop level can by far exceed the tree level contributions [26] and shift the KK-modes away from their tree level expectations. As an example, figure 2.1 illustrates the contribution coming from the violation of Lorentz invariance in five dimensions at loop level. This correction results from particles traversing from one side of the finite orbifold to the other. As a consequence of the loop corrections, KK-number

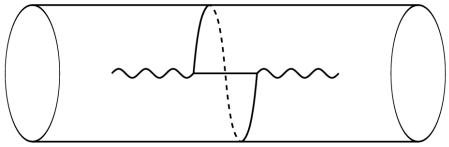

Figure 2.1: Loop violating Lorentz Invariance in 5 dimensions. The wavy line on the surface of the cylinder at each side of the loop, represents a particle propagating in ordinary 3+1 space-time. By propagating in the extra dimension (loop), it can be clearly seen that the starting and the finishing point of the loop do not overlap and Lorentz Invariance is therefore violated. [26]

conservation breaks and changes to KK-parity conservation ($P_{KK} = (-1)^n$ for the $n^{th}$ KK-mode [25]). Servant and Tait ( [27]) motivate an electrically neutral and non-baryonic particle as the most suitable LKP. Therefore, the most promising DM-candidates in UED are given by the first KK-excitations of the neutral gauge bosons, which are an analogue to the SM photon and $Z$ boson. In the SM, EWSB induces mixing between the gauge eigenstates of the gauge bosons $B$ and $W$. As a consequence, the mass matrix in UED in

the $(B^{(n)}, W_3^{(n)})$ basis for the $n^{th}$ excitation can be written as ( [25]):

$$\begin{pmatrix} \frac{n^2}{R^2} + \frac{1}{4}g_1^2v^2 + \delta M_1^2 & \frac{1}{4}g_1g_2v^2 \\ \frac{1}{4}g_1g_2v^2 & \frac{n^2}{R^2} + \frac{1}{4}g_2^2v^2 + \delta M_2^2 \end{pmatrix} \tag{2.11}$$

$g_1$ and $g_2$ are the $U(1)$ and $SU(2)$ gauge couplings and $\delta M_1^2$ and $\delta M_2^2$ the radiative corrections to the $B^{(1)}$ and $W^{(1)}$ masses. $v \approx 174$ GeV is the Higgs vacuum expectation value (VEV). In this notation, the SM neutral gauge bosons $(\gamma, Z)$ can be described by the mass matrix in the $(B^{(0)}, W_3^{(0)})$ basis. Hence, the mixing angle between the KK gauge bosons is the Weinberg angle, if one neglects the radiative corrections $\delta M_1^2$ and $\delta M_2^2$. The LKP is introduced in [27] in the limit of $\delta M_2^2 - \delta M_1^2 \gg g_1g_2v^2$, which minimises the mixing angle and maximises the diagonal entries in the mass matrix. Thus, the LKP is stable under decay and expected to consist of entirely $B^{(1)}$. Its coupling to the SM fermions is given by $g_1$, and is therefore proportional to the fermion's hypercharge.

There are also other possible natural choices for LKP candidates with UED, like the KK 'graviton', the KK 'neutrino' or the $Z^{(1)}$ boson that may constitute viable DM candidates. They are not considered here. Instead, this thesis focuses on the most promising KKDM prospect in terms of indirect detection expectations, the KK 'photon', $B^{(1)} = \gamma^{(1)}$. The here considered UED models with five spacetime dimensions are characterized by two parameters: the LKP mass, $m_{\gamma^{(1)}}$, and the mass splitting $\Delta_{q^{(1)}} \equiv (m_{q^{(1)}} - m_{\gamma^{(1)}})/m_{\gamma^{(1)}}$, where $m_{q^{(1)}}$ is the mass of the first KK quark excitation [22, 27–29]. The pair annihilation of $B^{(1)}$ into ordinary matter must preserve momentum and all involved symmetries, expressed in the conservation of quantum numbers, in the same way as SM particles. The KK-Parity, $P_{KK}$, introduced in section 2.6, arises as an additional symmetry, much like R-parity in the MSSM. The LKP described as the KK 'photon' is a boson and hence, the pair-annihilation into SM particles is allowed. Table 2.1 summarizes the branching ratios for all possible annihilation channels. It also accounts for the Higgs-field annihilation channel ($\Phi\Phi^*$) that is neglected in this analysis, due to its small branching ratio but high degree of uncertainty. In the approximation that all heavier KK-particles have the same mass as the LKP ($\Delta_{q^{(1)}} = 0$), the relative branching ratios are determined only by the hypercharges of the final fermion states [30]. Table 2.1 lists in addition to the branching ratios for $\Delta_{q^{(1)}} = 0$ also the numbers for $\Delta_{q^{(1)}} = 0.14$, corresponding to the case of less degenerate LKP model.

For the work, described in more detail in paper II (attached to this thesis), the theoretical KK model space for spin dependent cross sections and muon

Table 2.1: LKP annihilation branching ratios for two values of $\Delta_{q^{(1)}}$ [30]. Ratios are not summed over generations. Channels within parenthesis give negligible contribution to a neutrino flux from the Sun. The Higgs-field annihilation channel, marked with $^\dagger$, is neglected, due to large uncertainty and small contribution to the neutrino flux.

| Channel | Branching ratio | |
|---|---|---|
| | $\Delta_{q^{(1)}} = 0$ | $\Delta_{q^{(1)}} = 0.14$ |
| $(e^+e^-), (\mu^+\mu^-), \tau^+\tau^-$ | 0.20 | 0.23 |
| $(u\overline{u}), c\overline{c}, t\overline{t}$ | 0.11 | 0.077 |
| $(d\overline{d}), (s\overline{s}), b\overline{b}$ | 0.007 | 0.005 |
| $\nu_e\overline{\nu}_e, \nu_\mu\overline{\nu}_\mu, \nu_\tau\overline{\nu}_\tau$ | 0.012 | 0.014 |
| $(\Phi\Phi^*)^\dagger$ | 0.023 | 0.027 |

fluxes from the Sun in terms of WIMP mass were derived from Refs. [28] and [30] with the use of DarkSUSY [19].

## 2.7 Current Experimental status of Dark Matter searches

Despite several widely discussed observations, which resulted in a claim to have observed possible DM signatures, no undisputed experimental evidence for WIMPs exists. Two examples of such claims are shown in figures 2.2 and 2.3, and explained in more detail below. Experimental efforts are generally divided into direct detection experiments, searching for the possible nuclear recoil of the interaction of a WIMP within the detector volume, and indirect experiments, targeting the detection of radiation or secondary particles from WIMP annihilations. Scattering processes of WIMPs on nuclei can be classified in elastic or inelastic scattering and spin dependent or spin independent scattering. In the case of elastic scattering in a target material, the WIMP interacts with the nucleus as a whole, depositing a certain fraction of energy as nuclear recoil. In inelastic scattering processes, the WIMP interacts with the electrons of the target nucleus, ionizing the medium, or with the nucleus itself, leaving it in an excited state. The cross section for spin independent scattering, also called scalar scattering, increases with the atomic number of the experimental material, $A$, as $\sigma_{SI} \sim A^2$. Axial-vector interactions (spin dependent, $\sigma_{SD}$) result from couplings of the spin content of the WIMP to the total spin component of the target material. Therefore, $\sigma_{SD}$ is proportional to $J(J+1)$, where $J$ is the total nuclear spin of the target

nuclei.

direct detection

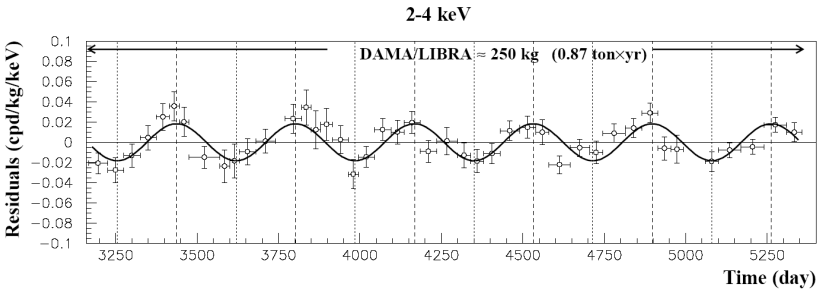


Figure 2.2: Model-independent residual rate of the single-hit scintillation events, measured by the DAMA/LIBRA [31] experiment in the (2 – 4) keV energy intervals as a function of the time. Figure is taken from Ref. [32].

Direct detection experiments currently set the most stringent limits on $\sigma_{SI}$. Techniques vary between experiments to exploit the signature of a nuclear recoil within a certain detector medium, which ideally consists of heavy nuclei to enhance $\sigma_{SI}$ and also has a large spin component for probing $\sigma_{SD}$ most efficiently. Three common techniques are used individually or in combination: measuring heat, in form of phonons, scintillation and ionization. Detectors applying an event-by-event based analysis are always utilizing two methods in parallel. Liquid Xenon detectors, like XENON and XENON100 [33, 34] and ZEPLIN-II [35] use scintillation and ionization, whereas cryogenic detectors, based on semiconducting materials such as Germanium and Silicon, e.g. CDMS-II [36] and EDELWEISS-II [37], use heat and ionization. The analysis strategy of these combination experiments is to use the reduced ionization or scintillation relative to the heat signal for nuclear scattering events relative to electromagnetic induced backgrounds. An additional event-by-event based experimental technique are bubble chambers, used by COUPP [38] and PICASSO [39]. A second strategy for direct experiments to separate signal from background, is to look for an annual variation of the rate. Such an modulation can arise due to the Earth's annual motion around the Sun within the galactic reference frame. Under this effect, the orbital motion of the Earth adds and subtracts depending of the season an additional component towards the total velocity. The expected WIMP-recoil rate increases for higher WIMP velocities. The DAMA/LIBRA [31] and NaIAD [40] experiments, measuring scintillation in Sodium Iodine, focus on the detection of the

annual modulation. The DAMA/LIBRA collaboration has observed such an annual variation as shown in figure 2.2, and reports that their measured modulation is consistent with detection of WIMPs with approximately 60 GeV mass and a total cross section of the order of $10^{-41}$ cm$^2$ [32]. CDMS, XENON and EDELWEISS have explored the DAMA favored parameter space without finding evidence of DM. Thus, the DAMA discovery remains a highly controversial claim that seems to be difficult to reconcile with other experiments.

## indirect detection

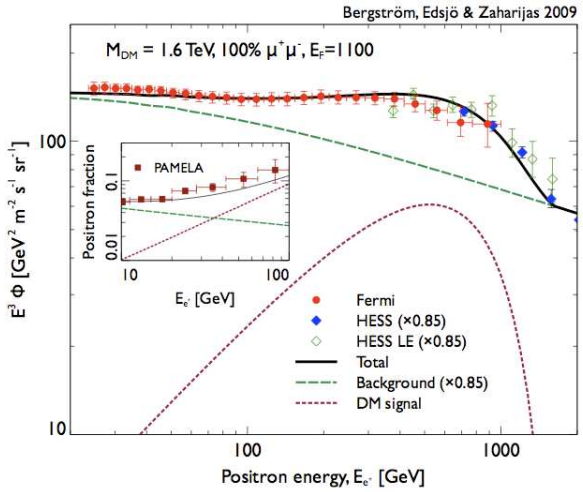


Figure 2.3: Spectra for a good fit DM model. The signal and background are shown for electrons ($e^+e^-$) together with measurements from Fermi [41] and H.E.S.S data.(taken from [42])

A complementary search for the nature of DM is through various indirect detection experiments. Sections 2.5 and 2.6 showed that the here considered WIMP candidates, $\chi$ and $\gamma^{(1)}$, can pair annihilate and their annihilation products, like neutrinos, gamma rays, positrons and antimatter nuclei, can be detected. WIMPs in galactic halos may scatter and slow down, to become gravitationally trapped in large celestial bodies, enhancing their density and thus, their probability of annihilation. Section 2.8 will discuss details of using the Sun as a potential source of neutrinos, originated from WIMP annihilations. A flux of highly energetic neutrinos can be detected in large neutrino telescopes such as Baikal [43], SuperKamiokande [44], ANTARES [45],

AMANDA [46] and IceCube [47]. Such an increased flux of high energy neutrinos above background from celestial bodies would be a so-called 'smoking gun' signal, as would monoenergetic gamma lines from annihilations. These gamma lines and the continuous gamma spectrum, resulting from decay of secondary annihilation products from WIMP annihilations within e.g. the galactic center or halo, may be observed by satellites like Fermi [48] or ground based air Cherenkov telescopes, e.g H.E.S.S. [49], VERITAS [50], MILAGRO [51] and the future CTA [52]. Resulting positron and antimatter fluxes may be measured by satellite detectors, such as PAMELA [53] and the recently launched AMS detector [54]. Fermi, reported an increased positron flux at high energies above expected backgrounds [41]. This observation is consistent with a signal resulting from annihilation of WIMPs in the TeV range, as shown in figure 2.3 (taken from Ref. [42]). Ref. [42] add on top of the expected background flux a component arising from direct annihilation of 1.6 TeV WIMPs into $\mu^+\mu^-$ pairs to explain the observed spectrum (note, other WIMP scenarios are also feasible). This possible hint for DM can convincingly be explained by standard astrophysical phenomena, like pulsars or supernova remnants [55], but DM cannot strictly be ruled out as explanation.

## 2.8 Indirect Solar Search for WIMP Dark Matter

Assuming that the local DM-density in our galaxy is about $\rho_{local} = 0.3$ GeV/cm$^3$ [25], each liter of our Milky Way would contain on an average between 0.01 and 1 WIMP particles. While traveling through the galaxy, WIMPs can scatter off nuclei in stars or planets and become trapped within their deep gravitational wells. Once trapped within such a gravitational potential the WIMP's trajectory is similar to that of a comet. Each successive scattering process results in a loss of energy and the WIMP gradually describes trajectories closer and closer to the object's core. Thus, the WIMPs can be expected to accumulate in the core of the object to densities that exceed $\rho_{local}$ by several orders of magnitude. The principle of an indirect search demands a relatively highly efficient annihilation of WIMPs into particles detectable on Earth. The solar search that is performed in this thesis with the neutrino telescope IceCube [47] looks for an enhanced $\nu_\mu\overline{\nu}_\mu$ flux out of the core of the Sun, which arises from WIMP annihilations.

## Accumulation in the Sun

In the case of our solar system, WIMPs can scatter via two different processes off nuclei in the Sun. One is the spin-independent interaction with contributions from the spin-independent component of the WIMP-on-proton elastic scattering cross section and the elastic scattering cross section of WIMPs on higher elements. The composed spin-independent capture rate, $C_{SI}^{\odot}$ (eq. 2.13), is found to be three to four orders of magnitude smaller than the spin-dependent capture rate, $C_{SD}^{\odot}$, in equation 2.12, accounting for the spin-dependent component of the WIMP-on-proton elastic scattering [56], when only taking Hydrogen and Helium into account - as these are the most abundant elements in the Sun. Recent studies indicate the important contribution of heavier elements to the total scattering probability, despite their diminutive abundance [57], as they enter the calculation of the cross section $\sim A^2$.

$$C_{SD}^{\odot} \simeq 3.35{\cdot}10^{20} s^{-1} \left(\frac{\rho_{\text{local}}}{0.3\,\text{GeV}\,\text{cm}^{-3}}\right) \left(\frac{270\text{km}\,\text{s}^{-1}}{\overline{v}_{\text{local}}}\right)^3 \left(\frac{\sigma_{H,SD}}{10^{-6}\text{pb}}\right) \left(\frac{100\,\text{GeV}}{m_{DM}}\right)^2 \tag{2.12}$$

$$C_{SI}^{\odot} \simeq 1.24 \cdot 10^{20} s^{-1} \left(\frac{\rho_{\text{local}}}{0.3\,\text{GeV}\,\text{cm}^{-3}}\right) \left(\frac{270\text{km}\,\text{s}^{-1}}{\overline{v}_{\text{local}}}\right)^3 \left(\frac{100\,\text{GeV}}{m_{DM}}\right)^2 \times \left(\frac{\sum_i n_i \sigma_{N_i,SI}}{10^{-6}\text{pb}}\right) \tag{2.13}$$

With $\sigma_{H,SD}$ being the spin-dependent elastic scattering-cross section for WIMP-on-hydrogen, $\overline{v}_{\text{local}}$ the root mean square (rms) of the local velocity of dark matter in the halo ($\sim$ 270 km s$^{-1}$), and $m_{\text{DM}}$ the mass of the DM particle. The spin-independent elastic scattering-cross section of solar elements, $N_i$, is given in eq. 2.13 as $\sigma_{N_i,SI}$, where $n_i$ include information on the solar abundances of elements, dynamical factors and form factor suppression [3]. The total solar accretion is calculated to $C_C^{\odot} = C_{SD}^{\odot} + C_{SI}^{\odot}$. The velocity distribution of relic WIMPs within the potential well of the Sun is assumed to follow a Maxwellian distribution, peaking at $\overline{v}_{\text{local}}$ [58]. It can be seen in eq. 2.12, 2.13 that the process of WIMP capture within the Sun or more general in celestial bodies, is more sensitive to the lower end of the WIMP velocity spectrum and heavily dependent on the local mean DM density (e.g boost factor).

The annihilation cross section times the relative WIMP velocity ($v$) per volume, $A^{\odot}$, is given in equation 2.14, where the effective core volume of the sun for WIMPs, $V_{eff}$, is approximated by matching the sun's temperature with

the gravitational potential energy of one WIMP at the core radius [3],

$$A^{\odot} = \frac{\langle \sigma v \rangle}{V_{eff}} \ . \tag{2.14}$$

In order to reach equilibrium between the annihilation rate, $\Gamma_A$, and the capture rate, $C_C^{\odot}$, the relative number of WIMPs, $N$, has to remain constant. Therefore the rate of change of this number, $\dot{N}$, given in equation 2.15 has to be zero,

$$\dot{N} = C_C^{\odot} - A^{\odot} N^2 \stackrel{!}{=} 0 \ . \tag{2.15}$$

The present annihilation rate, $\Gamma_A$, is given by [3] as,

$$\Gamma_A = \frac{1}{2} A^{\odot} N^2 = \frac{1}{2} C_C^{\odot} \cdot \tanh^2 \left( t_{\odot} \sqrt{A^{\odot} C_C^{\odot}} \right) \tag{2.16}$$

where $t_{\odot} = 4.5$ billion years is the age of our solar system. In order to fulfill equation 2.15, the hyperbolic tangent in equation 2.16 is required to be equal to one. Thus, in order to reach equilibrium between the annihilation rate and capture rate of WIMPs in the sun the following relation has to be valid:

$$t_{\odot} \sqrt{A^{\odot} C_C^{\odot}} \gg 1 \tag{2.17}$$

For most WIMPs within the allowed mass range, relation 2.17 can be confirmed, and hereafter it is assumed that the Sun either reaches or nearly reaches the above described equilibrium [30]. In equilibrium, the annihilation rate only depends on $C_C^{\odot}$, and thus, only on the total scattering cross-section.

## Annihilation of WIMPs and resulting Neutrinos

Neutrinos are the only particles that are able to leave the Sun without being completely absorbed. Thus, the direct neutrino channels provide a definite source of monochromatic neutrinos, along with the very short lived particles, which form a secondary source of neutrinos when decaying. Particles created in annihilations to light quark pairs have long enough lifetimes to interact and loose energy before they decay. Neutrinos resulting from decay chains of shorter lived quark pairs ($b\overline{b}$, $t\overline{t}$ and $c\overline{c}$) have a 'soft' spectrum. Annihilations into $W^+W^-$ results in a 'hard', higher energy, spectrum, through the secondary direct decay process into charged leptons and neutrinos, $W^{+(-)} \rightarrow l^{+(-)} + \nu_l(\bar{\nu}_l)$. Below the $W^{\pm}$ mass, the annihilation into $\tau^+\tau^-$ is assumed as the channel producing the highest energy neutrinos. The primary annihilation spectrum is extremely different between $\chi$ and $\gamma^{(1)}$. For

the LKP, branching ratios are fixed from theory, and therefore a distinct 'real' annihilation spectrum can be simulated, whereas every MSSM model will result in a different set of branching ratios. Since it is too time consuming to perform an analysis for every possible annihilation channel and spectrum, the two end points of the spectrum are chosen, i.e the 'soft' $b\bar{b}$ and 'hard' $W^+W^-$ ($\tau^+\tau^-$ below 80.2 GeV) channels. Within the work, described in paper II, it was noted that the resulting muon spectra at the detector per LKP annihilation is extremely similar to the one of the hard $\chi$-channel, see figure 2.4. Consequently, the analysis described in this thesis is optimized for the above described hard and soft channel, focusing on $\chi$ searches. But, the event selection for the hard $\chi$ channel is also optimal for LKP searches, due to their similar muon spectra at the detector.

Charged current (CC) interactions with the solar medium are the dominant processes that reduce the flux of neutrinos from WIMP annihilations in the core of the Sun. Muon and electron neutrinos, reacting with the protons in the Sun, create electrons and muons, which are instantly absorbed. Taus, produced in CC reactions of tau neutrinos, decay again into a tau neutrino of less energy, conserving the original number of generated tau neutrinos. The probability of neutrinos escaping the sun rises significantly for lower energies [30], see figure 2.5. Additionally, $\nu_\mu \leftrightarrow \nu_\tau$ oscillation randomizes an outgoing muon or tau neutrino flux sufficiently, so an average of both components is expected at the detector [3]. Electron neutrino components, due to oscillation, occur only at energies much lower than those investigated here.

### solar WIMP neutrino signal

IceCube analysis, looking for WIMPs, focus on data that are taken during the austral winter. In this period, the Sun is below the horizon at the South Pole and its maximum declination is equal to the obliquity of the ecliptic, 23.4°. The solar zenith angle distribution as observed from the South Pole is plotted in figure 2.6 for the period of two years, indicating the time when the Sun is below the Horizon, as well as the IceCube 79-string detector uptime. The 79-string detector was commissioned by the $31^{st}$ of May, resulting in an approximate uptime of $\sim$ 100 days during the austral winter 2010 and additional uptime in 2011 till the start of the full IceCube 86-string detector. Fig. 2.6 additionally shows the period with the Sun being above the Horizon. This period is potentially used to extend the traditional solar WIMP analysis and increase hereby the detector livetime. The sketch in figure 2.7 exempli-

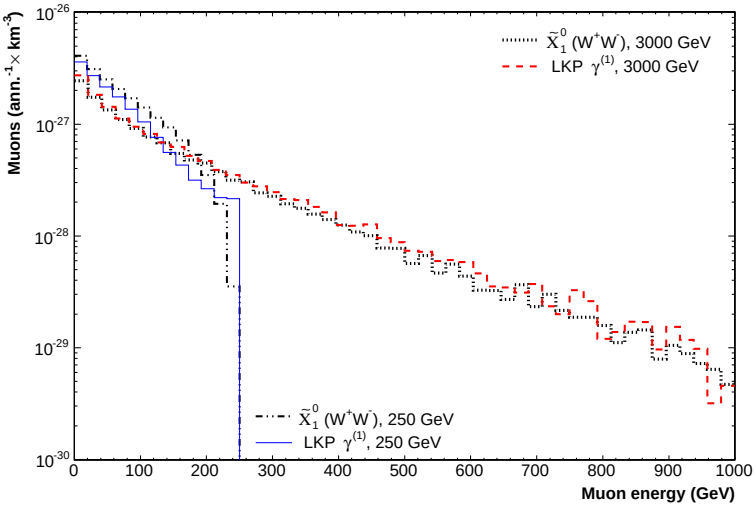


Figure 2.4: Comparison of simulated muon spectra from LKP, $\gamma^{(1)}$, and neutralino, $\tilde{\chi}_1^0$, annihilations observed in IceCube, for two WIMP masses, 250 and 3000 GeV, representing the boundaries of the investigated LKP model space.

fies the solar WIMP analysis with the IceCube neutrino detector with its two major background components, atmospheric muons, $\mu_{atm}$, and atmospheric neutrinos, $\nu_{atm}$. Potential background sources for this search are discussed in detail in chapter 4. As indicated in figure 2.7, the $\mu_{atm}$ zenith range is restricted to angles, $\Theta < 90°$, whereas $\nu_{atm}$ constitute a nearly isotropic background over the whole sky.
The search method applied in this thesis aims at detecting WIMP annihilations indirectly by observing an excess of high energy neutrinos from the direction of the Sun above the $\nu_{atm}$ background (see detailed discussion on background sources in chapter 4).

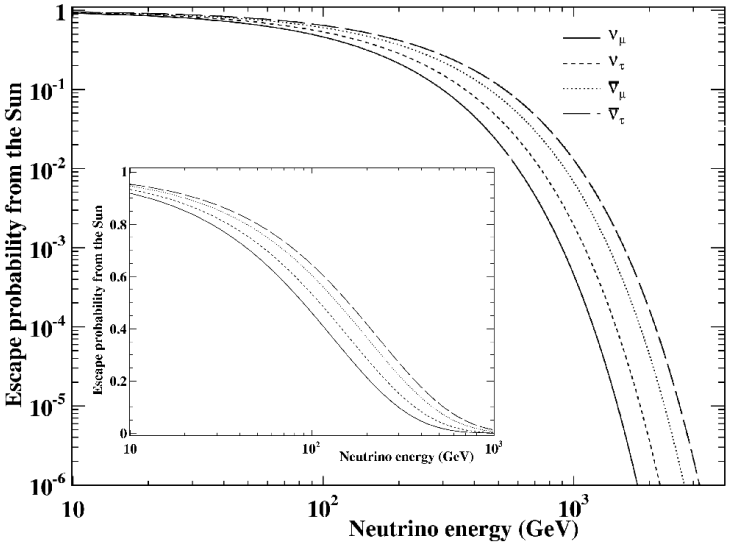


Figure 2.5: Escape probability of neutrinos from the Sun. Muon neutrinos ($\nu_\mu\bar{\nu_\mu}$) and tau neutrinos ($\nu_\tau\bar{\nu_\tau}$) are modeled as indicated within the legend. The zoom-in figure illustrates the escape probability in linear scale for lower neutrino energies.

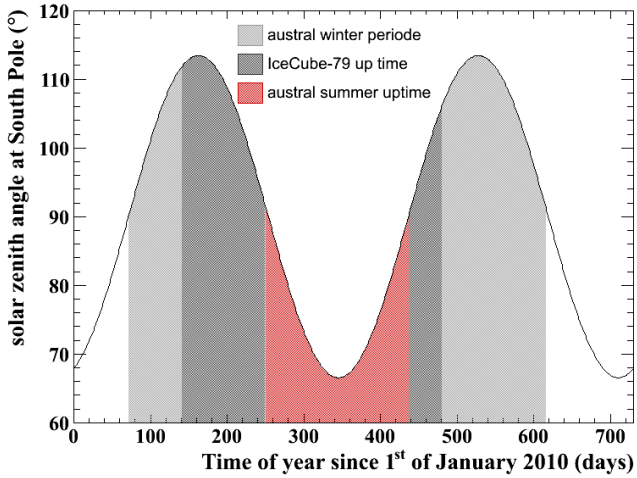


Figure 2.6: Zenith angle distribution to the Sun as viewed from the South Pole as a function of time. The austral winter, as well as the IceCube 79-string detector uptime during this period, is indicated, along with the austral summer period in red.

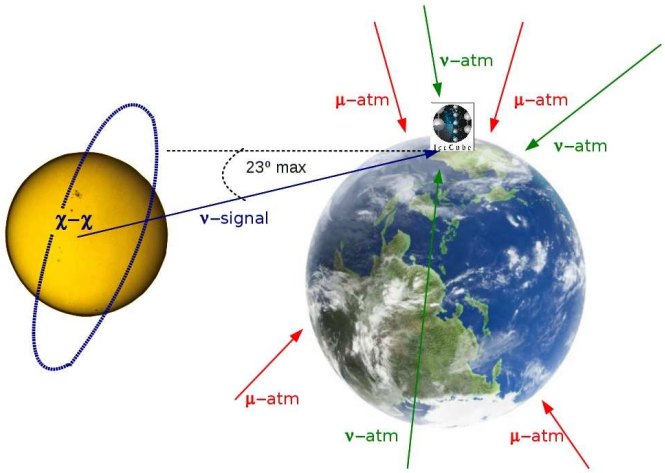


Figure 2.7: Sketch illustrating the search method for a solar WIMP neutrino signal in IceCube. Atmospheric muons, $\mu_{atm}$, and neutrinos, $\nu_{atm}$, are created in air showers in the Earth's atmosphere by cosmic ray interactions with nuclei. $\mu_{atm}$ can only come from above the detector, due to the limited muon range in matter. Muons created nearby the detector in CC reactions from $\nu_{atm}$ have no angular limitation. Signal source neutrinos only come at a maximum declination of $\Theta < 23.4°$ below the horizon at the South Pole.

# Chapter 3

# High energy neutrino detection

Neutrinos are weakly interacting fundamental particles with very little mass, if any at all, and no electrical charge. Therefore, neutrinos can only be observed in extremely large detector volume or over a very long observation time. High energy neutrinos, like the potential indirect DM signal from the Sun, are best studied with neutrino telescopes, that use a large instrumented detector volume. IceCube in its 79-string configuration will nearly use a full cubic kilometer of Antarctic ice in an open detector geometry, detecting the Cherenkov light radiated by passing charged leptons that are produced in interactions with nuclei inside or close to the detector.

## 3.1 Neutrino-nucleon interactions

Neutrinos interact with nuclei in the ice through two different channels. The charged current interaction (CC) and the neutral current (NC) interaction, can be summarized in the following equations:

$$\nu_l(\overline{\nu}_l) + N \rightarrow l^-(l^+) + X \quad (CC) \tag{3.1}$$
$$\nu_l(\overline{\nu}_l) + N \rightarrow \nu_l^{'}(\overline{\nu}_l^{'}) + X \quad (NC) \tag{3.2}$$

$N$ is the initial nucleus and $X$ the final hadronic remains of the nucleus, usually a hadronic cascade, also called a hadronic shower. The NC interaction occurs through the exchange of the neutral $Z$ boson, and can in fact be regarded as a scattering of the initial neutrino on the nucleus $N$. Hadronic showers can result in detectable charged leptons at high energies, but do not contribute at the targeted energies of this study of $10^1$ GeV $\sim 10^3$ GeV. This

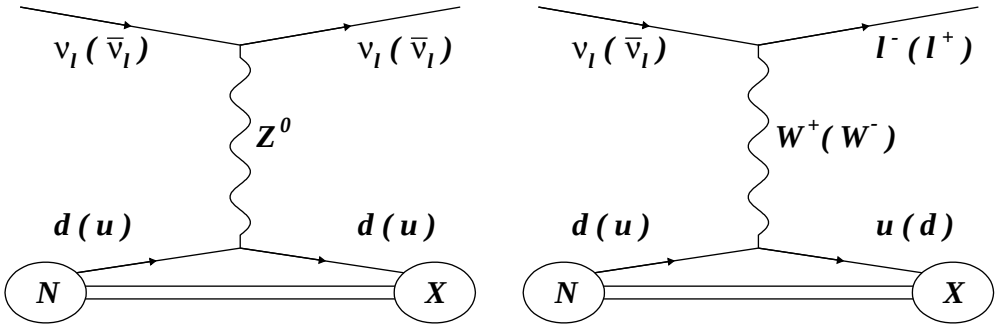


(a) NC interaction (b) CC interaction

Figure 3.1: The left Feynman diagram illustrates the $NC$ interaction of $\nu_l(\overline{\nu_l})$ of all flavors with a nucleon $N$. The right Feynman diagram stands for the $CC$ interaction, creating a charged lepton $l^-(l^+)$. In both diagrams, $X$, is the final hadronic remains of $N$.

also applies to the hadronic cascades, $X$, produced in the CC interaction, where charged $W$ bosons are exchanged. Both processes are summarized in the Feynman diagrams of figure 3.1. Of all charged leptons produced, only the muons travel through the detector medium for up to several kilometers, radiating Cherenkov light (see section 3.3). Electrons, roughly 200 times lighter than muons, typically lose their energy in electromagnetic showers within a few meters in ice, which makes them only detectable at energies above the GeV range. Produced tau leptons decay with a very short lifetime of less than 1 ps into the following secondary particles [59]:

$$\tau^-(\tau^+) \rightarrow X + \nu_\tau(\overline{\nu}_\tau) \tag{3.3}$$
$$\rightarrow \nu_\tau(\overline{\nu}_\tau) + \overline{\nu}_e(\nu_e) + e^-(e^+) \tag{3.4}$$
$$\rightarrow \nu_\tau(\overline{\nu}_\tau) + \overline{\nu}_\mu(\nu_\mu) + \mu^-(\mu^+) \tag{3.5}$$

While muons are produced in the third channel, such tau events are neglected, as only a small fraction of the kinetic energy is transferred to the muon produced via equation 3.5. For the simulated signal, $\mu^+$ and $\mu^-$ created in CC interactions from $\overline{\nu}_\mu(\nu_\mu)$ are the only particles considered in this analysis to trigger the detector.

The CC interaction is a deep inelastic scattering process of neutrinos of energy $E_\nu$ with a nucleus, $N$, of mass $M_N$. This is expressed with the double

differential cross sections [60]:

$$\frac{d^2\sigma^{CC}_{\nu N}}{dxdy} = \frac{2 \cdot G_F^2 M_N E_\nu}{\pi} \cdot \left(\frac{M_W^2}{Q^2 + M_W^2}\right)^2 \cdot \left[xq(x,Q^2) + x(1-y)^2\bar{q}(x,Q^2)\right] \quad (3.6)$$

$$\frac{d^2\sigma^{CC}_{\overline{\nu}N}}{dxdy} = \frac{2 \cdot G_F^2 M_N \overline{\nu}}{\pi} \cdot \left(\frac{M_W^2}{Q^2 + M_W^2}\right)^2 \cdot \left[x(1-y)^2 q(x,Q^2) + x\bar{q}(x,Q^2)\right] \quad (3.7)$$

Here, $M_W$ is the W boson mass and $G_F$ is the Fermi constant, $q(x,Q^2)$ and $\bar{q}(x,Q^2)$ are the parton distribution functions for the quarks and antiquarks depending on the momentum transfer $Q^2$. $x$ and $y$ are the Bjorken scaling variables defined as,

$$x = \frac{Q^2}{2 \cdot\ M_N \cdot\ (E_\nu\ -\ E_\mu)} \qquad \text{and} \quad y = \frac{E_\nu\ -\ E_\mu}{E_\nu} \quad . \qquad (3.8)$$

The variable $x$ is the fraction of the momentum of the nucleus carried by the quark and $y$ is the fraction of neutrino energy transferred to the quark. Both scaling variables determine the degree of inelasticity of the interaction. Equations 3.6 and 3.7 differ only in their dependence on $y$ in the quark and anti quark parton functions. At low energies, where the parton functions are dominated by the valence quarks, the deep inelastic neutrino cross section for scattering on protons in Antarctic ice is two to three times larger for the neutrino than for the antineutrino. This is due to helicity suppression of the anti neutrino reaction. As a result the CC interaction of the anti-neutrino is suppressed by a factor $(1-y)^2$ for energies below $\sim 10$ TeV [7]. At very high energies, the cross section is no longer dominated by the valence quarks but by the sea quarks, which are always produced in $q\overline{q}$ pairs. Consequently, both cross sections become equal.

The mean angle between the initial neutrino and the muon path is approximated with equation 3.9 [61] and shown for the targeted signal energy range in figure 3.2 (a). Above $\nu$-energies of 100 GeV the directional information of the initial neutrino is well retained. Below 100 GeV the restriction in angular precision from kinematics will be more challenging. At this lowest part of the investigated energy spectrum, quality cuts within the analysis select predominantly events where most of the energy went into the created muon. This creates a selection effect, boosting the angular precision even at lowest possible energies. This is shown for the total solar WIMP signal at final filter level for the IceCube-86 sensitivity study in figure 3.2 (a). Note, the scattering angle does not correspond to the quality in angular reconstruction.

$$< \Theta^2_{\nu\mu} > \approx \frac{0.7^\circ}{(E_\nu/\mathrm{TeV})^{0.7}} \qquad (3.9)$$

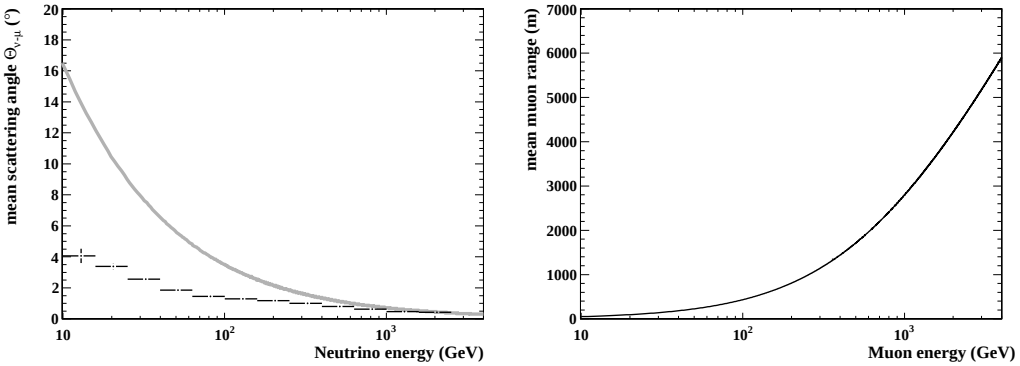


(a) mean scattering angle (b) muon range

Figure 3.2: Mean scattering angle between initial neutrino and created muon as a function of neutrino energy, estimated with eq. 3.9 from [61], is shown as the thick gray line (left plot). Also shown in black data points, the selection effect at final filter level of the IceCube-86 sensitivity study, improving the kinematic angle. The bin width is indicated and the statistical error of each bin shown in vertical bars. Mean muon range in ice as a function of muon energy, calculated with eq. 3.11, taken from [62] (right plot).

## 3.2 Muons in ice

While passing through the detector, energy losses for muon energies $E_\mu \sim 1$ TeV are dominated by four processes. Ionization, described by the Bethe-Bloch formula, is nearly energy independent at the GeV range and above, and occurs continuously along the trajectory of the muon [63]. Energy losses through bremsstrahlung, pair production of $e^+e^-$ and photo-nuclear interaction, are energy dependent and can therefore be used for energy reconstructions above the threshold energy, $E_{th}$ (see figure 3.3). In equation 3.10 all energy dependent contributions of the muon losses are expressed in one parameter $b(E_\mu) \approx 3 \cdot 10^{-4}\mathrm{m}^{-1}$. Whereas ionization is described by the parameter $a(E_\mu) \approx 0.2$ GeV m$^{-1}$ [63],

$$-\frac{dE_\mu}{dx} = a + b \cdot E_\mu \quad \text{and} \quad E_{th} = \frac{a}{b} \; . \tag{3.10}$$

The average energy loss due to Cherenkov radiation of approximately $\sim 1$ keV/m, as calculated below, is not a dominant source of energy loss of a muon in the ice, but the crucial one for its detection within Cherenkov detectors. The resulting muon range, $R_\mu$, for muons at energies below $\sim 10$ TeV can be approximated with equation 3.11 [62], which leads to a muon range of

more than 200 m even for a 50 GeV muon (note that the diameter of the DeepCore sub-array is 150 m). The approximated muon range is illustrated in figure 3.2 (b).

$$R_\mu \approx \frac{1}{b}\ln\left(\frac{E_\mu}{E_{th}} + 1\right) \tag{3.11}$$

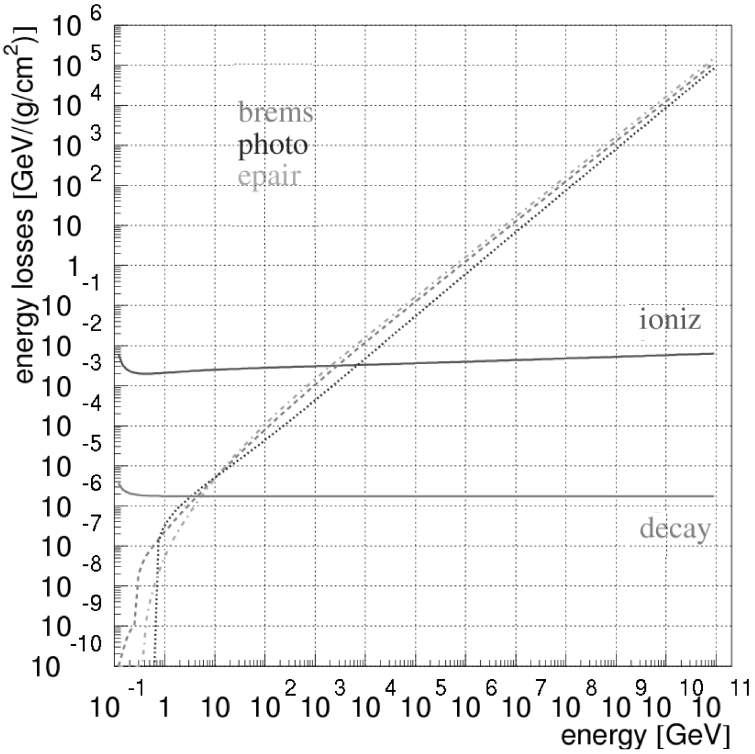


Figure 3.3: Contributions of the different processes leading to muon energy losses in ice as a function of $E_\mu$: decay losses (lower solid line), ionization (upper solid line), bremsstrahlung (dotted line), photo-nuclear (fine dotted line), and pair production of $e^+e^-$ (dash-dotted line) [64].

## 3.3 Cherenkov radiation

The Cherenkov effect occurs when a charged particle travels through a dielectric medium with speed, $v$, higher than the speed of light in that particular medium, i.e., when $v > c/n$ ($n$ is the index of refraction of the medium).

Charged particles like the produced leptons polarize the surrounding medium. Due to a particle speed being above the speed of light, the polarization is anisotropic along the velocity axis. Therefore the emitted moving light cone is shaped like a Mach cone. The cone front has an opening angle, $\Theta$, with the velocity axis, which is energy dependent [65].

$$\cos\Theta_{H^2O} = \frac{c_M}{\nu} = \frac{1}{n(\lambda)\cdot\beta} \tag{3.12}$$

At targeted energies (ultra relativistic limit $\beta = 1$) the opening angle of the cone in water or frozen water (ice) is $\Theta_{H^2O} = 41.2°$, since to first order the refracting index $n = 1.33$ for the visible electromagnetic spectrum. The Cherenkov photon emission is slightly wavelength dependent and rises with shorter wavelengths. The number of photons, $N_{vis}$, emitted due to the Cherenkov effect by a particle of charge $Z \cdot e$, per unit wavelength and unit length can be estimated with the Frank-Tamm expression [66]:

$$\frac{d^2N_{vis}}{dx\ d\lambda} = \frac{2\pi\ z^2\alpha}{\lambda^2}\left(1 - \frac{1}{\beta^2 n^2(\lambda)}\right)\ . \tag{3.13}$$

Here, $\alpha = 1/137$ is the fine structure constant. A characteristic value for the number of photons emitted by a muon, derived by integrating equation 3.13 over the sensitive range [$\sim$ 300nm,$\sim$ 600nm] of the photo multiplier tubes (PMT) and glass spheres enclosing the PMT, is $\sim 330$ per cm track length. This corresponds to an average energy loss due to Cherenkov radiation of $\sim 1$ keV/m.

## 3.4 Propagation of light in the South Pole ice

Light propagation in the deep ice at the South Pole is possible over large distances as the ice is extremely clear and pure. Knowledge of the optical properties of South Pole ice at depths greater than 1400 m, where the ice is significantly clearer and contains only very few air bubbles, is essential. The ice is modeled with the so-called six-parameter ice model introduced in Ref. [67]. This model describes the ice by a table of parameters $b_e(400)$, $a_{dust}(400)$, related to scattering and absorption at 400 nm, and temperature $\delta\tau$, given for each ice layer (assuming layers of 10-meter width), and by six parameters that were fitted in Ref. [67] to AMANDA data. The currently used ice-model within IceCube is a direct fit approach to fitting the ice properties, called SPICE-MIE, which also includes a new improved parameterization of mie scattering [68]. A global fit is performed to a set of

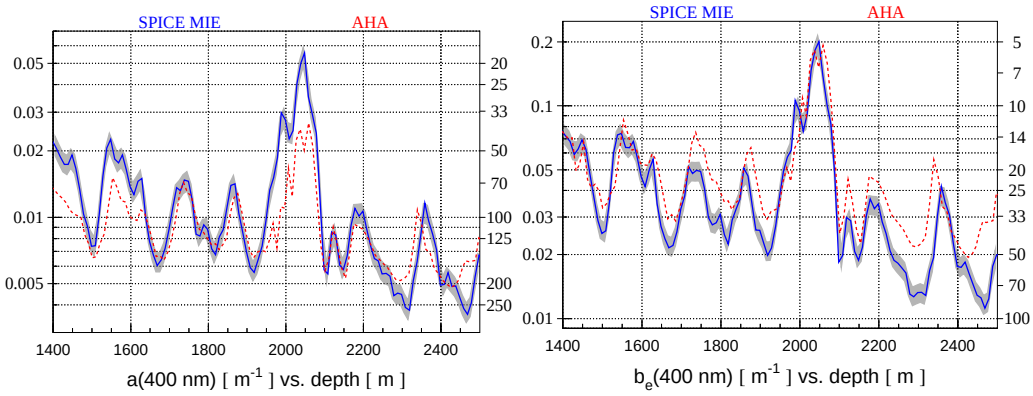


Figure 3.4: Values of $b_e(400)$ and $a(400)$ vs. depth for converged solution in solid blue. The updated model of [67] (AHA) is in dashed red. The scale and numbers to the right of each plot indicate the corresponding effective scattering $1/b_e$ and absorption $1/a$ lengths in [m].

data with in-situ light sources covering all depths of the detector, resulting in a single set of scattering and absorption parameters of ice, which describes these data best [69]. Figure 3.4 shows the obtained best fit solution for absorption and scattering length versus depth at the South Pole, and compares with the previously used AHA (Additionally Heterogeneous Absorption) ice-model [67]. The large peaks in absorption and scattering, and hence the layered structures within the ice, result from the so-called dust layers. The plots indicate extremely clear ice in the bottom of the detector, the DeepCore sub-array region, with an effective absorption length up to 250 m and an effective scattering length up to roughly 90 m.

# Chapter 4

# Background sources

The experimental background in the IceCube 79-string detector is largely dominated by atmospheric muon events, $\mu_{atm}$, from above the South Pole. Although $\mu_{atm}$ trigger roughly $\sim 10^5$ times more often than atmospheric neutrinos, $\nu_{atm}$, their angular distribution makes rejection very efficient. $\nu_{atm}$ can travel through Earth unhindered and are therefore indistinguishable from signal events. This scenario is illustrated in figure 2.7 in section 2.8.

## 4.1 Atmospheric muons

Cosmic Rays (CRs), consisting predominantly of protons, $p$, alpha particles, $He^{2+}$, and electrons, $e^-$, but also heavier ionized atoms, that are believed to be accelerated in various astrophysical phenomena, produce highly energetic, ultra relativistic muons in reactions with molecules in the Earth's atmosphere. The top panel in figure 4.1 shows the CR flux as a function of particle energy, as measured by various air-shower detectors [70]. Muons, created in the resulting air showers, can penetrate the East Antarctic Ice Sheet up to several kilometers deep. The dominant production of muons is via the leptonic or semi-leptonic decays of charged pions or kaons, through the following decay chain,

$$p^+(He^{2+}, \text{etc.}) + \text{N} \rightarrow \pi^\pm(K^\pm) + \pi^0 + \text{X} \ , \tag{4.1}$$

$$\pi^\pm(K^\pm) \rightarrow \mu^\pm + \nu_\mu(\bar{\nu_\mu}) \ , \tag{4.2}$$

$$\mu^\pm \rightarrow e^\pm + \nu_e(\bar{\nu_e}) + \bar{\nu_\mu}(\nu_\mu) \ , \tag{4.3}$$

$$\pi^0 \rightarrow \gamma\gamma \ , \tag{4.4}$$

where N stands for the initial molecule and X for the hadronic remains of the interaction. The average trigger rate of around 2400 Hz for the 79-string detector is entirely dominated by $\mu_{atm}$. The $\mu_{atm}$ energy spectrum follows, in first order, the initial power law spectrum of CRs, which is proportional to $E^{-2.7}$ [71]. $\mu_{atm}$ are constrained to a zenith angle range of $0° < \Theta < 90°$. Thus, $\mu_{atm}$ show up as strictly down-going events and can be efficiently rejected by directional cut selections (note, this is neglecting the effect of mis-reconstructed muon tracks).

## 4.2 Atmospheric neutrinos

CR interactions in the atmosphere also create high energy neutrinos, $\nu_{atm}$, in decays of secondary air shower particles like $\pi^{\pm}(K^{\pm})$(see eq. 4.2), $\mu^{\pm}$(see eq. 4.3) and other mesons. In the GeV-range, their energy spectrum follows the CR power law spectrum, proportional to $E^{-2.7}$. At energies above 1 TeV, the interaction length of the secondary particles becomes shorter than the decay length, resulting in a steepening of the spectrum ($\propto E^{-3.7}$) [73] (see bottom panel figure 4.1). The angular distribution is not perfectly isotropic as the initial CR spectrum might indicate. The horizontal component is slightly enhanced compared to the vertical component. This anisotropy is caused by the non-uniform atmospheric density profile. Particle path lengths in less dense upper layers are increased for horizontally moving particles, whereas for vertical particles, path lengths are decreased. In addition to the conventional component of the atmospheric neutrino spectrum, defined via eq. 4.2 and 4.3, a prompt component is predicted from the semi-leptonic decay of charmed particles, hadrons with c-quark content [74]. $\nu_{atm}$ are the dominant background at higher filter levels for this analysis.

## 4.3 Neutrinos from the solar atmosphere

Cosmic rays may interact in the atmosphere of the Sun in the same way, described in section 4.1, as when entering Earth's atmosphere. The produced particles propagate through the Sun until they either decay or produce new particles in secondary interactions (eq. 4.1 with 4.4). The main contribution to a detectable neutrino flux component comes from decays of $\pi^{\pm}$, $K^{\pm}$ and $\mu^{\pm}$. As the solar atmosphere is less dense at typical interaction heights than that of the Earth, a larger fraction of the mesons will decay instead of interacting, enhancing the $\nu$-flux component from the solid angle of the solar

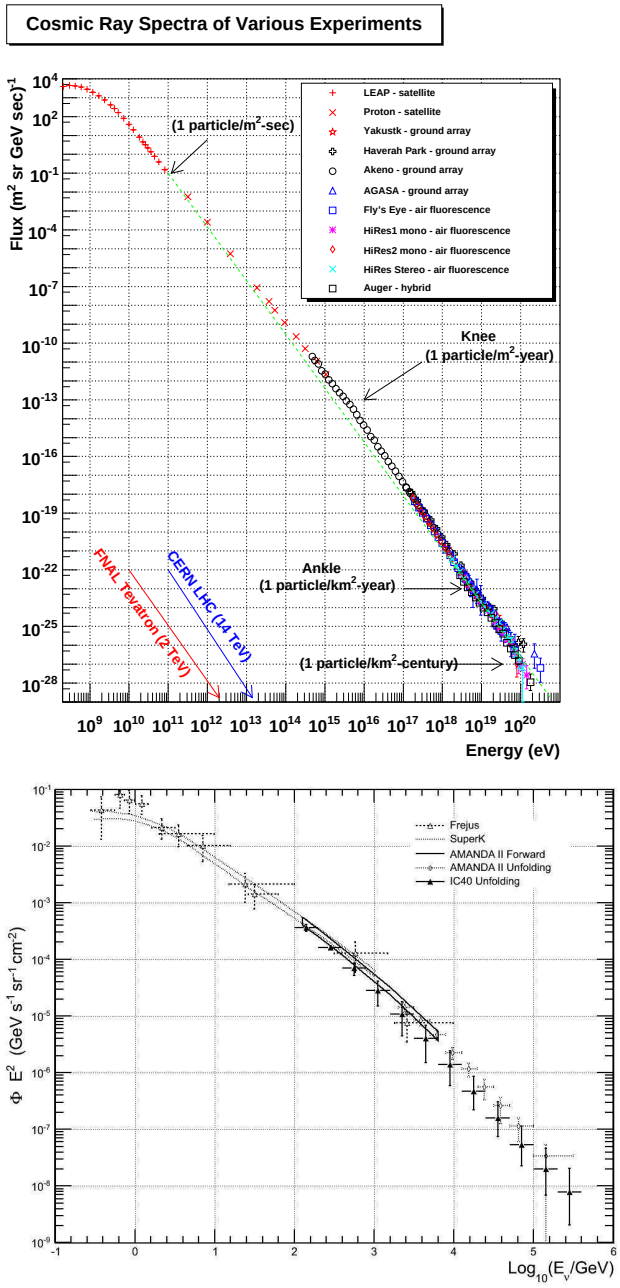


Figure 4.1: Flux of primary CRs as a function of energy [70] (top panel), and measurements of the atmospheric neutrino spectrum [72] (bottom panel).

disc [75]. This $\nu$-flux component describes an indistinguishable background for potential DM annihilation $\nu$-signals from the center of the Sun.
To calculate the number of expected events from this background within the

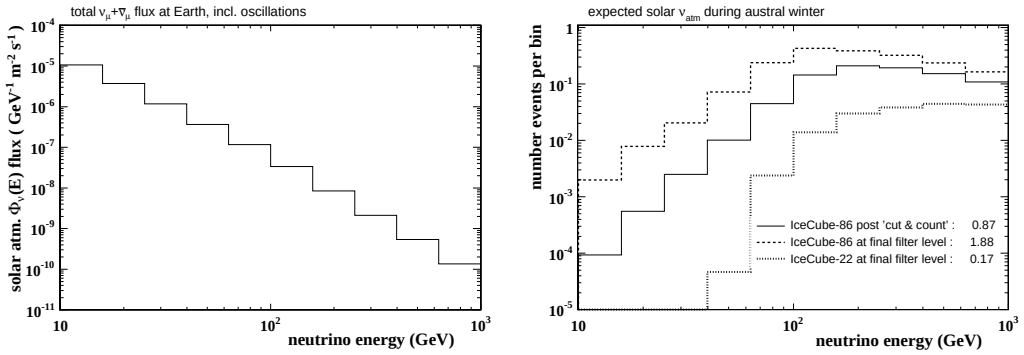


(a) solar atm. $\nu$-flux (b) predicted number of events in IceCube

Figure 4.2: Left panel shows the solar atmospheric $\nu$-flux, $\Phi(E_\nu)$, with respect to $E_\nu$, integrated over the solar disc, as predicted by [76]. Number of predicted IceCube events per austral winter per $\nu$-energy bin is shown in the right panel for the IceCube 22-string case and two different IceCube 86-string cases.

IceCube 79-string configuration, the predicted solar atmospheric neutrino fluxes [75, 76] are binned in $\nu$-energy within the sensitive energy range of the analysis from $\sim$ 10 GeV to $\sim$ 1 TeV (shown for Ref. [76] in figure 4.2 (a)). The number of expected events per energy bin during one austral winter, as shown for three different cases in figure 4.2 (b), is derived by multiplying the $\nu$-flux with the final $\nu$-effective area and integrating over energy and time. The $\nu$-effective areas for the IceCube-86 string configuration, are taken at final filter level (before and after an optimized directional cut on the solar position) of the IceCube 86-string solar WIMP sensitivity study, whereas the IceCube 22-string $\nu$-effective area is taken from attached paper II.
The total number of expected neutrinos from the solar atmosphere varies depending on the predicted flux ( Ref. [75] or [76]) between 1 and 3 events for the time of a full austral winter period within the full IceCube detector array. The derived numbers for the IceCube 22-string configuration of less than 1 event are in agreement with the unblinded analysis result, detailed in Ref. [1] and attached paper II.

## 4.4 Galactic neutrinos

Galactic neutrinos are a result of CR interactions with interstellar gas in the galactic disk. The created neutrino flux contributes at very high energies

above 100 TeV to the total neutrino background [77]. At lower energies, the contribution is negligible. Generally, neutrino detectors in the Southern Hemisphere are not ideally positioned for neutrino sources situated in the Southern celestial Hemisphere, like the galactic center.

## 4.5 Cosmological neutrinos

### GZK effect

CRs with energies above $6 \cdot 10^{19}$ eV are energetic enough to produce a delta resonance in the reaction with a photon from the CMB [78]. Equations 4.5 and 4.6 describe the ultra high energy neutrino production resulting out of this resonance.

$$p + \gamma \rightarrow \Delta^+ \rightarrow \begin{cases} n\pi^+ & (1/3) \\ p\pi^0 & (2/3) \end{cases} \tag{4.5}$$

$$\pi^+ \rightarrow \nu_\mu + \mu^+ \rightarrow \nu_\mu + e^+ + \nu_e + \bar{\nu_\mu} \tag{4.6}$$

The created diffuse ultra high energy neutrino flux is modeled to be very low and is also afflicted with a high degree of uncertainty, due to little knowledge about the origins of ultra high energy cosmic rays, and is consequently not considered here.

### Point source neutrinos

Point sources other than the Sun are possible sources of background neutrinos. Theoretical models describing gamma ray bursts (GRBs), super nova remnants (SNR), and active galactic nuclei (AGN) predict the production of neutrinos [77]. Nevertheless, the estimated diffuse neutrino fluxes are too low to play an important role in the composition of the total neutrino background. Supernova explosions could possibly be detected in the IceCube neutrino telescope by an excessive rise of the background noise within the entire array over the blast duration caused by the large flux of low energy neutrinos. Generally, these $\nu$'s do not constitute a potential background source for the analysis discussed here with expected $\nu$-energies far below the individual detection threshold in the MeV range [77].

# Part II

# Experimental Overview

# Chapter 5

# IceCube neutrino observatory

The IceCube neutrino observatory is a neutrino telescope deployed deep in the East Antarctic Ice Sheet at the geographical South Pole, close to the Amundsen-Scott station (see figure 5.1 for a schematic view). The optical sensors are arranged in a three-dimensional lattice along cables ('strings') and are directed downwards towards the center of Earth, thereby minimizing atmospheric background from above (see section 4).

## from Amanda to IceCube

AMANDA, the Antarctic Muon And Neutrino Detector Array, is the predecessor of IceCube at the South Pole and was decommissioned during the 2008-09 polar season after more than a decade of operation. The first AMANDA strings were deployed during the Austral summer 1993-1994 at depths between 800 m and 1000 m. It was found that at these depths the concentration of air bubbles is too high to reconstruct muon tracks. This detector prototype is called AMANDA-A. At depths lower than 1400 m, the ice is significantly clearer and contains less air bubbles. As a consequence of the discovered ice properties, all 19 AMANDA strings (AMANDA-A is not regarded as part of AMANDA) were deployed at depths below 1200 m, in the years 1995 to 2000. String 17 is the only exception, because of deployment problems [79].

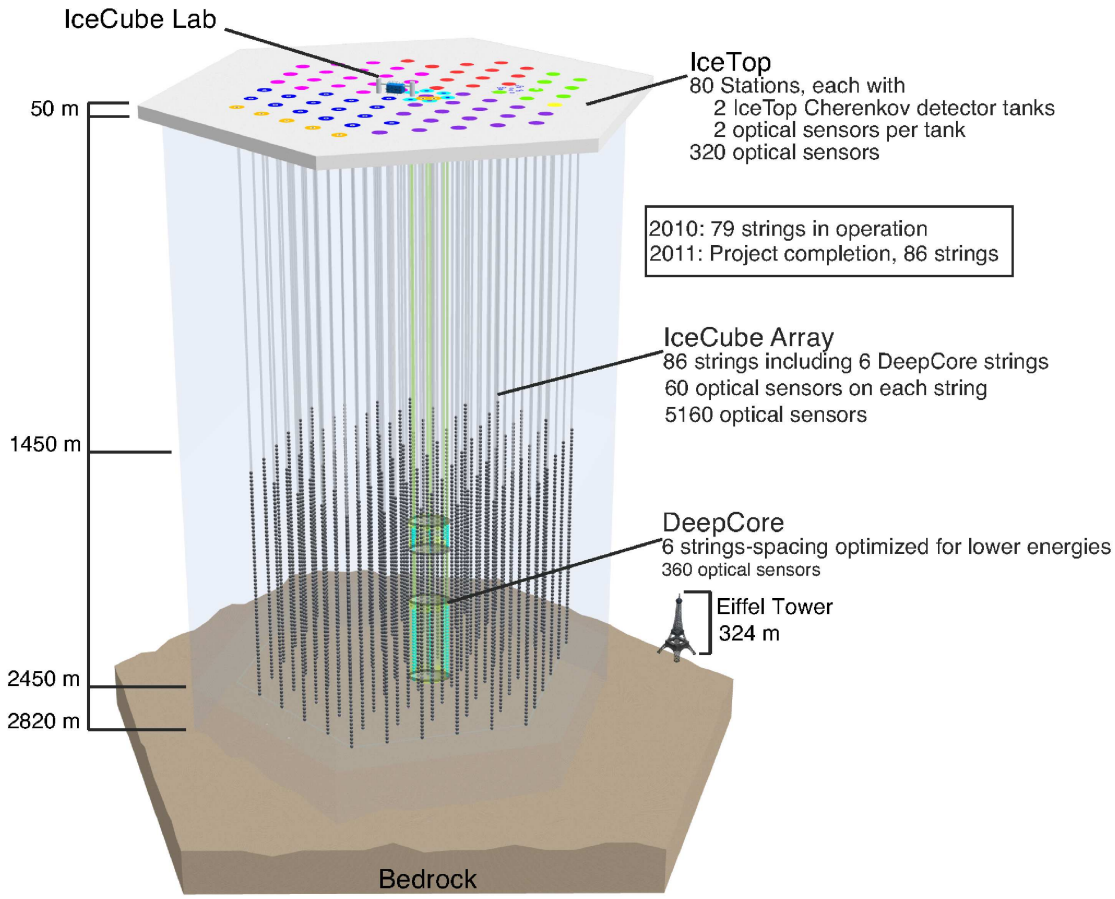


Figure 5.1: Three dimensional overview of the 79-string IceCube 2010 detector with the location of the DeepCore array marked in the center, bottom of the detector. IceTop stations are at the surface at each string location. The missing 7 final strings are shown in orange.

## 5.1 IceCube

The neutrino observatory IceCube, which was completed on the 18th of December 2010, consists of 5160 digital optical modules (DOMs) installed on 86 strings between 1450 m and 2450 m below the surface [81]. IceCube with a horizontal spacing of 125 m and vertical spacing of 17 m, has an instrumented volume of 1 $km^3$. Its design is optimized for the detection of high energy astrophysical neutrinos with energies above $\sim$ 100 GeV. The horizontal surface layout and the depth profile of the IceCube 79-string detector is shown in

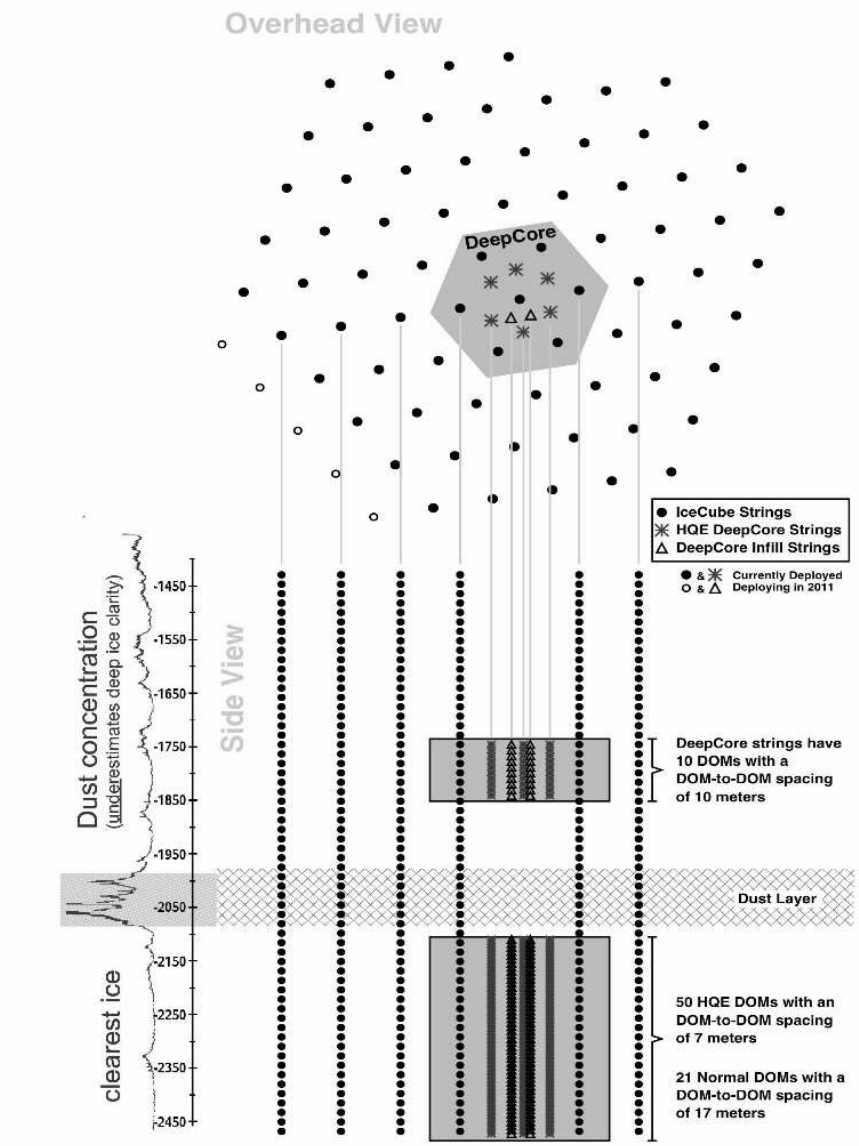


Figure 5.2: Top and side view of the IceCube detector. Deployed strings within the IceCube 79-string detector are marked in solid circles, whereas unfilled circles indicate strings deployed during the 2010-2011 season. DeepCore string positions are marked with stars. Different DOM spacings are indicated on the strings. Also shown is the main dust layer within the detector and a dust concentration profile as measured with the dust logger [80].

figure 5.2. Within the figure, DOM locations in depth are contrasted to the dust concentration within the South Pole ice.

## 5.2 sub-detectors

Within the IceCube 79-string detector, 73 strings are 'standard' IceCube strings with an intra-string DOM spacing of 17 m and 6 strings are DeepCore strings, explained below.

### DeepCore

The DeepCore sub array is a denser array of 6 strings surrounding the IceCube center string (string 36). The distance to neighboring strings is less than 75 m and between break-outs on each string 7 m below the dust layer and 10 m above. This array forms a dense core of DOMs within the clearest part of the ice, and increases the sensitivity to low energy neutrinos below 100 GeV. The standard IceCube photo multiplier tube (PMT), discussed in section 5.3, is exchanged for high quantum, HQ, efficiency PMTs with a 40% higher quantum efficiency within the DOMs. Spacing and position of DeepCore DOMs and strings relative to 'standard' IceCube are shown in figure 5.2. Within the 79-string configuration, the 'in-fill' strings 79 and 80 that form an even more dense array within the 6 DeepCore strings, as indicated in figure 5.2, are not yet deployed.

### IceTop

The IceTop surface air shower array consists of pairs of tanks placed at the top of each 'InIce' string and separated from each other by 10 m. Each tank is instrumented with two DOMs frozen into the top of the ice in the tanks. The tanks contain a reflective coating to improve the chance of capturing Cherenkov light, generated by charged particles passing through the tanks. In contrast to the IceCube 'InIce' detector, IceTop does not aim to detect neutrinos. Typical signals, from individual muons or bundles of multiple muons, are much bigger than signals in the deep ice. In order to reduce noise background, both IceTop tanks within one station are operated in coincidence mode. IceTop is predominantly used in CR composition studies but also acts as a surface veto for the 'InIce' detector for extremely bright down-going CR

shower events.

## 5.3 IceCube digital optical module

The optical modules consist of a pressurized 13 mm thick glass sphere containing a downwards orientated photo multiplier tube (PMT), a 2 kV high voltage power supply for the PMT and a DOM Main Board (MB). The PMT (Hamamatsu R7081-02) is 25 cm in diameter and in contact with the glass through a transparent silicone gel. The PMT has 10 dynodes with a total amplification strength in the order of $10^7$, allowing accurate single photon detection. The glass spheres are transparent for light with wavelengths between 300 nm and 600 nm and have a transmission maximum at 410 nm [79, 82]. The MB additionally contains a LED flasher board, which is used for in-situ time, charge and position calibrations of the DOMs within the detector array. The LEDs emit a calibrated light pulse that can be detected with receiving DOMs surrounding the emitter. In contrast to the AMANDA OMs, the IceCube DOMs operate as completely autonomous data acquisition modules by digitizing the pulse information within the module (in-ice digitization). All modules are remotely controlled, independent of each other, and synchronized by a master clock system, the reciprocal active pulsing system, RAPcal. The RAPcal method coordinates an ensemble of over 5000 free running clocks with respect to a GPS disciplined reference to establish a common time-base for all created hits in data [83]. Therefore, the digital optical modules (DOMs) timestamp each pulse with the actual 'in-ice' time information. The pulse information sent to the surface is not susceptible to cross talk or dispersion like previously the analogue AMANDA signal. IceCube PMTs detect Cherenkov photons by creating analogue charge signals, which are digitized by a fast Analog-to-Digital converter (FADC) and a set of three advanced transient waveform digitizers (ATWDs) on the MB. The ATWDs contain three channels with gains of $\frac{1}{4}$, 2 and 16 [79]. The ATWDs sample 128 bins of 3.3 ns width, whereas the FADC samples at a rate of 40 MHz for a time window of 6.4 $\mu$s. These raw IceCube data contain time stamped and digitized waveforms of the measured charge pulses. The average PMT waveform, an example is shown in figure 5.3, is composed from individual waveforms that are caused by different processes within the PMT. The pre-pulse is ascribed to photoelectrons ejected from the first dynode and thereby missing the first amplification step and therefore, occurring some tens of ns earlier than the main peak. Pre-pulses are seen in less than 1% of the single-photoelectron (SPE) rate [84]. Figure 5.3 shows that the

prompt response to a light pulse has a tail extending to about 100 ns after the initial rise of the main pulse. Afterpulses are seen in the range of 300 ns to 11 $\mu$s. Such afterpulses are attributed to ionization of residual gases by electrons accelerated in the space between dynodes [84]. Ions created in this way can be accelerated back to the photo-cathode, causing ejection of electrons which are subsequently amplified like the original photoelectrons. Up to primary pulses of $1 \cdot 10^6$ p.e.,6% of the charge is delivered in the interval from 300 ns to 11 $\mu$s [84]. In addition to these PMT effects, thermal

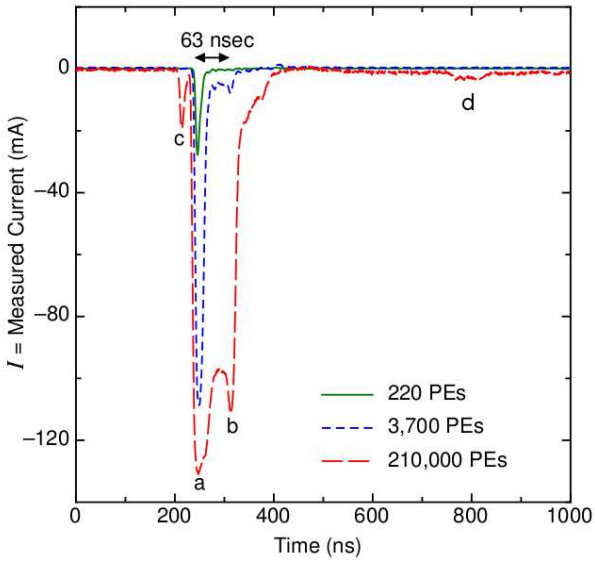


Figure 5.3: Average waveforms observed in a PMT for 3 ns laser light pulses with progressively higher intensity: (a) main peak; (b) secondary peak due to unusual electron trajectories, like inelastic scattering on dynodes (late pulses); (c) pre-pulse; (d) after-pulse. (figure taken from [84])

electrons evaporate from the photo cathode and dynodes causing the dark noise of the PMT. Radioactive decays within the glass sphere are an additive component to the dark noise. The total dark noise rate of the 'standard' IceCube DOM is 700 Hz and 900 Hz for the HQ PMT within the DeepCore DOMs. These noise pulses can not be distinguished from pulses caused by Cherenkov photons. As noise pulses occur randomly, coincidence conditions between adjacent optical modules help to reject noise pulses in data taking.

A DOM that records a hit sends a signal to the neighboring DOMs. This enables each DOM individually to check whether the detected hit fulfills the local coincidence (LC) condition, or if it is an isolated hit. For the

generally used LC span 2 setting, it is required that there is an additional DOM hit within two neighboring DOMs to the initially responding DOM in a maximum time frame defined by a time $t_{LC}$ of 1000 ns. DOMs fulfilling this LC condition are tagged with a so-called hard local coincidence, HLC. DOMs that record a hit without being in LC with the next to closest DOM, are isolated hits. These hits are often referred to as soft LC, SLC, hits, although they are in no coincidence at all. An SLC readout is reduced to only 3 samples out of the first 25 samples of the FADC (the highest amplitude bin and its two neighbors), instead of the full FADC and ATWD information in case of an HLC event.

## 5.4 Data acquisition

The IceCube trigger system is software based, since the DOM signals are already digitized. All DOM hits, as described in section 5.3, are sent to digital string processors (DSPs), one per detector string. The DSPs report all hits to a central trigger processor.

## 5.5 Trigger algorithm in IceCube-79

If there is a minimum of 8 hit DOMs within 5 $\mu$s, that fulfill the LC condition, IceCube is triggered. This basic multiplicity trigger is called simple majority trigger ($SMT8$). Within the DeepCore fiducial volume, consisting of the bottom 50 DOMs on the 6 DC string plus the bottom 22 DOMs on the 7 surrounding IceCube strings, $26, 27, 35, 36, 37, 45, 46$, a low threshold SMT trigger is applied for selecting low energy events. The $SMT3$ trigger is based on LC hits in the above defined group of DOMs, requiring 3 hit DOMs within a 2.5 $\mu$s time window. A third trigger algorithm, the string trigger, is designed to increase the sensitivity for vertically up-going low energy events. This is also based on LC hits and requires 5 hit DOMs within 7 adjacent ones on the same string, within a time window of 1000 ns. If one or multiple triggers are recorded, a global trigger is formed, containing all relevant information of the sub-triggers within a trigger hierarchy, e.g. trigger type, trigger time and trigger duration.

## 5.6 Trigger development studies

### 5.6.1 Cylinder trigger

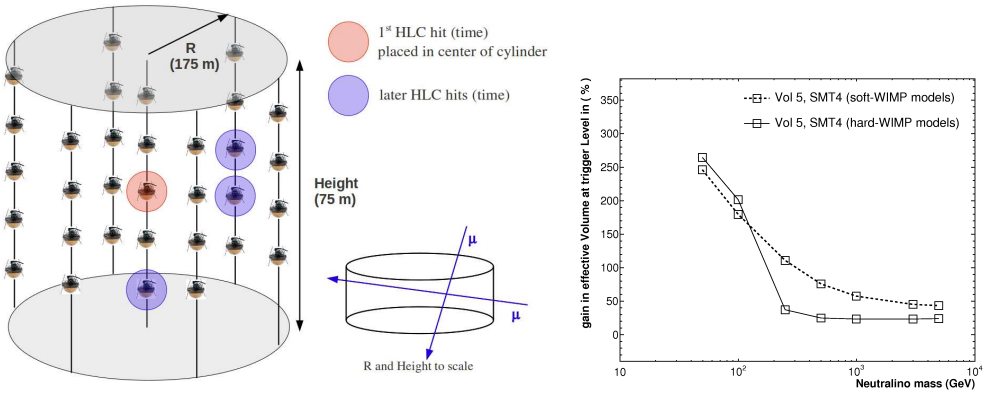


(a) CylinderTrigger (b) gain in effective Volume

Figure 5.4: Illustration of Cylinder Trigger. Improvement in the effective Volume for solar WIMP searches in percent for the proposed VT configuration for soft (dashed) and hard (solid) WIMP models.

The Cylinder trigger is designed to capture low energy horizontal events that would not trigger either $SMT8$ or a string trigger. Such events are expected to be important for low energy analyses such as solar wimp.

The trigger is intended to be part of the InIce trigger. The algorithm is split in two parts. First, a low-threshold time coincidence requirement is made, using a simple majority logic. For events that satisfy the timing condition, a positional analysis is applied. Here, each HLC hit is used as the center of a pre-defined cylindrical volume, in which all additional HLC hits that occur within 1000 ns are counted. If such a volume is found to contain enough hits, the trigger is satisfied (the threshold is set to 4 hits). The cylindrical volume contains seven strings, one central and the six nearest neighbors, defined by the cylinder radius $R = 175$m. The height of the cylinder is configured to 75 m. This corresponds to a total of five DOM layers, two up and down from the center layer, containing the original HLC hit that occurred first in time. Figure 5.4 (a) shows an illustration of the trigger implementation for the chosen cylindrical volume.

The best set of trigger parameters was found by varying the cylinder height and area, as well as the SMT threshold for the trigger. The SMT threshold

was varied between 4, 5, and 6. Cylinder heights corresponding to three, five, and seven DOM layers were tried. Figure 5.4 (b) shows the gain in effective volume for the hard and soft WIMP models for the chosen trigger settings in comparison to the situation without the Cylinder trigger.

The 2010 data was used to study, test and understand this new trigger algorithm, which was implemented for the start of the full IceCube-86 string detector in 2011. Figure 5.5 shows the distributions of COGz and Nchan for exclusive cylinder trigger events. In the current implementation, the Cylinder trigger has an exclusive trigger rate of 346 Hz in IceCube-86 string test runs and an exclusive low-Up filter rate of 13.75 Hz.

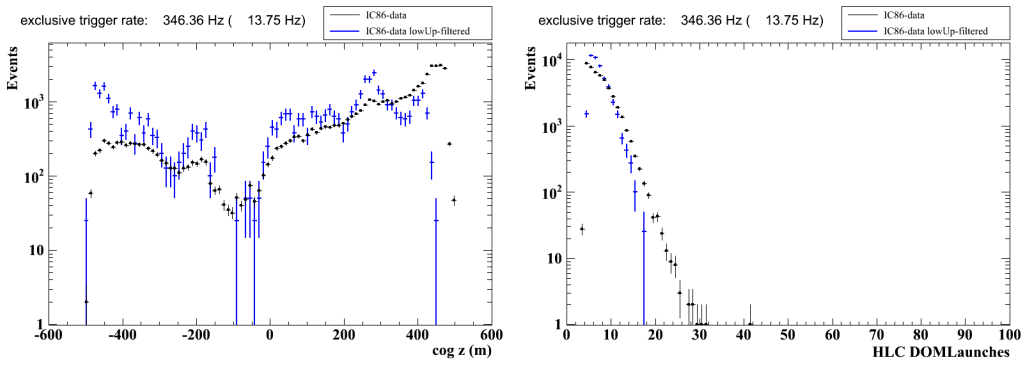


(a) COGz (b) Nchan

Figure 5.5: The COGz distribution (left) and Nchan (right) for exclusive Cylinder triggered events at trigger level and at low-Up filter level. Exclusive triggering events are shown in black, whereas exclusive low-Up filtered events are shown in blue. The filtered events are scaled for better comparison to the same number of events as the triggering events. Error bars are statistical.

### 5.6.2 Track engine trigger

With 86 strings, 60 modules per string, and 500 Hz of random pulses in each optical module (standard DOMs) the entire IceCube DAQ-system will experience an average of 2.6 MHz random hits per second. This is equivalent to around 13 hits in a $5\mu s$ time window. If one would demand 4 standard deviations above the average in a majority trigger, this would equate to at least 14.4 extra hits, which is unlikely for a low energy muon. By requiring hard local coincidences (HLC) between neighboring modules on the same string, the rate can be reduced. This however, leads to a loss of isolated hits.

A method to trigger on the full flow of hits without early restrictions using only topological features of a straight line, typical for muon track detection, is required. The Track Engine, TE, is an additional trigger for IceCube, specialized to trigger on low-energy muons (few hits per $\mu$-track). In the future, shower-like events or parallel tracks of more than one muon, may also be feasible topologies.

The TE is a device, which looks for correlations between pairs of hits (i.e. DOM launches). The main idea of the algorithm is to divide time in overlapping time windows of $5\mu s$; find all possible pairs of hits in each time window; calculate the spherical coordinates $\vartheta$ and $\phi$ (zenith and azimuth) of the relative position vectors of the hits of the pairs; histogram the angles; and look for peaks in the resulting 2d-histogram. Such peaks would indicate the presence of a track, whereas hit-pairs caused by noise should have a random distribution.

## The Track Engine Approaches TE-1 & TE-2

An FPGA implementation of the first Track Engine ambition level, TE-1, has been deployed during the South Pole season 2010/11. For all hit-pairs TE-1 looks at mainly four specific quantities: the distance ($d$) between DOMs; speed needed for a hypothetical particle to pass close each DOM in the pair at the time of the respective hit; $\vartheta$ and $\phi$. The speed of the hypothetical particle should be close to the speed of light (i.e. the speed of the high energy muon). The calculated speed will be approximate since the Cerenkov light will travel different distances before hitting a module. The ambition level, TE-2[1], will additionally use 3 impact parameter coordinates (Ip), where the Ip is defined as the point of closest approach of the projected infinite track, defined by the hit-pair, to the IceCube coordinate origin (center). Another quantity is the projected travel time, $\tau$, of a muon, from the hit-pair to the impact parameter. Quantities used in TE-1 and TE-2 are defined in figure 5.6.

[1]TE-2 is already in an advanced development stage but not discussed for deployment yet. It is one possible future upgrade

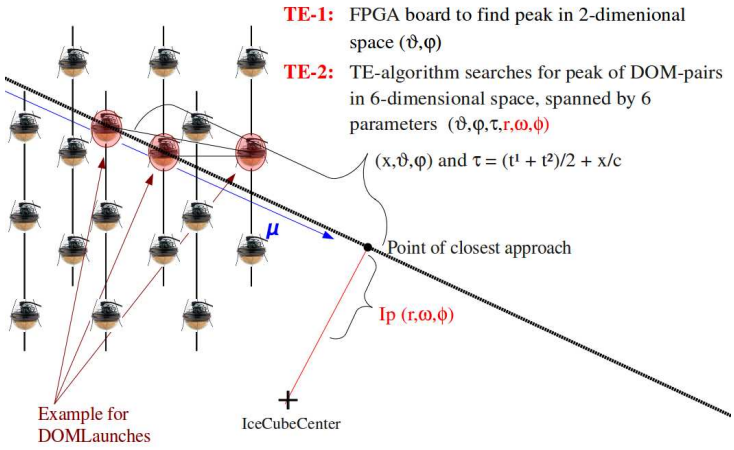


Figure 5.6: The definition of quantities used in TE-1 and TE-2. Red marks the additional impact parameter, Ip, coordinates.

## TE-1 implementation

In the TE-1 algorithm, a simple subdivision of the sphere into 344 almost uniformly sized bins is chosen to histogram the muon directions $\vartheta$ and $\phi$ (simple binning). Hardware (FPGA) and software use the exact same definition of bin boundaries. Separate test runs of the FPGA-board and the software-module on the simprod dataset 2488 (atmospheric $\nu$ simulation with a simulated $E^{-2}$-spectrum) have resulted in the same number of triggers. A flowchart of the TE-1 algorithm is shown in figure 5.7.

Suitable trigger settings are tested against the simulated MC truth value of a hit, i.e. noise or physics originated. This allows checks, whereby the trigger is only run on physics hits, or only on noise hits. The TE-1 algorithm can also be used as a first-guess track reconstruction.

## TE-1 impact on physics and global trigger rate

The number of "noise-only" triggers have been estimated for both systems. The expected rate for these random triggers for the IceCube-79 string detector configuration is evaluated from noise simulation to $< 5$ Hz. The increase in the number of triggering events for the TE-1 implementation are compared to the IceCube-79 standard triggers (SMT8, String, DC-SMT3) in figure 5.8 a, b and c. In addition, the effect of the Cylinder Trigger as discussed above

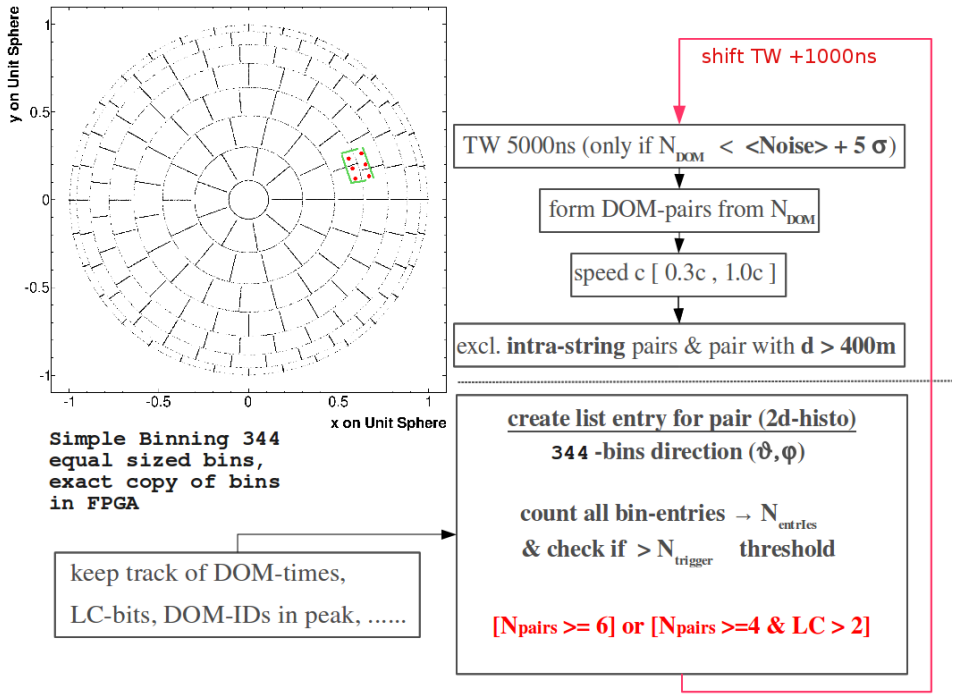


Figure 5.7: The simple binning subdivision of the sphere is shown in the top left. The flow chart diagram illustrates the TE-1 algorithm as used in software and FPGA. The actual trigger condition is marked in red.

is shown. A line demonstrating the capability of the TE-2 implementation is shown in 5.8 a and b.

| | corsika | $\nu_{atm} E^{-2}$ | WIMP 100 GeV soft |
|---|---|---|---|
| Volume Trigger | 9.8 | 54.9 | 106 |
| TrackEngine(TE-1) | 16 | 72.9 | 132 |
| low_up filter | 24.38 [Hz] excl. | N/A | ∼125 (non-DC events) |

Table 5.1: Summary of physics gain of TE-1 and VT. The increase in the number of triggered events is shown in percent (%), and calculated with IC79 triggers as frame of reference.

A summary of all numbers and improvements expressed in percent are given in table 5.1. The overlap of TE-1 and Cylinder trigger events, which are exclusive to the IceCube-79 triggers is roughly 50%. Improvement on the effective Volume after low-up-filter cuts when including also Cylinder trigger events are highlighted in figure 5.8 (d). To evaluate whether these events are "good" analysis events, the space angle between the true muon track and

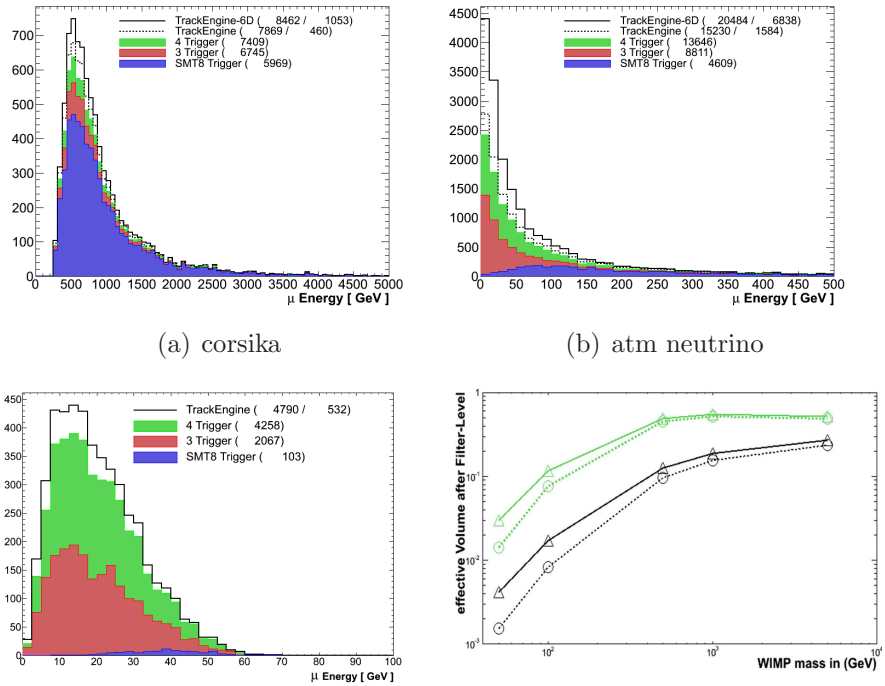


(a) corsika (b) atm neutrino

(c) WIMP 100 soft (d) WIMP after filter level

Figure 5.8: Figures (a), (b) and (c) show the accumulated number of triggered events according to legend. 3 triggers means all events triggered by IC79 triggers. The green area, indicating 4 triggers, also includes VT events. The dashed line in figures (a) and (b) represents the increased number of events when adding TE-1. The solid line in figures (a) and (b) represent TE-2. A line for TE-2 is not included in figure (c); therefore, the solid line shows the addition from TE-1. Figure (d) shows the effective Volume versus WIMP mass for soft (black) and hard (green) annihilation models. In both cases the dashed line with circles indicates the effective Volume without VT events. The solid lines with triangles show the increased eff. volume after filter level when including VT events. Figure (d) is also valid for TE-1 events, as the overlap of joint VT and TE-1 is 95%.

the reconstructed muon track is evaluated and shown for corsika (a) and $\nu_{atm}$ (b) datasets in figure 5.9. Each of these figures is normalized individually to the same number of entries in order to allow an accurate comparison of the different reconstructions. TE-1, indicated by the blue line and named FPGA-TE, and TE-2, indicated by the red line and named 6D-TE, are first guess reconstructions by themselves. Additionally, for the TE-1 events, the combined SLC+HLC pulses are extracted with seeded information from the

DOMs participating in the TE-1 trigger peak. For these exclusive events, the TE-1 direction is used as a seed for a simple 8-iteration llh SPE track fit (see chapter 6 for details on reconstruction algorithms). The SPE8-llh fits are indicated with black lines in figures 5.9 (a) and (b). Figure 5.9 clearly demonstrates the quality of the TE-1 exclusive events. Furthermore, the TE-1 seeded SPE8-llh fit highlights the potential of successful accurate track reconstruction at higher analysis levels with more sophisticated algorithms, e.g, hybrid reconstruction, as it improves the space angle distribution for inclusive as well as exclusive events for signal and background.

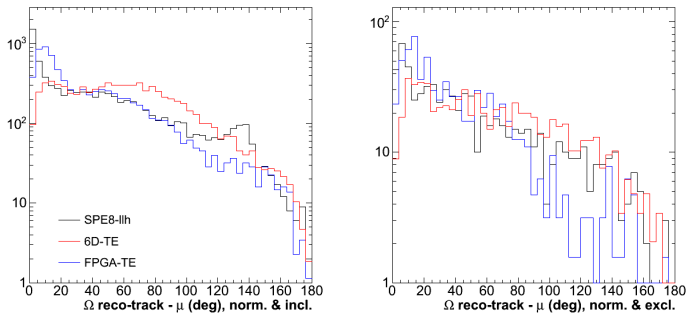


(a) corsika

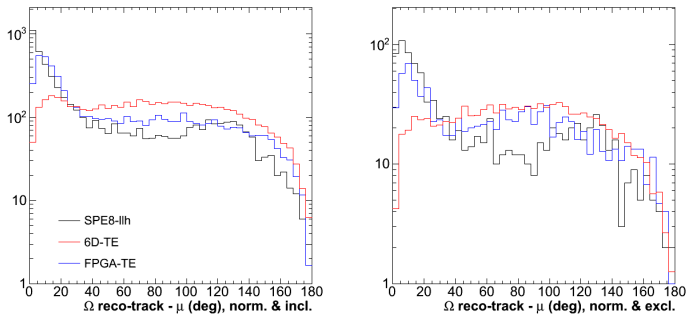


(b) atm neutrino

Figure 5.9: Space angle distributions of true MC $\mu$-tracks compared with reconstructed $\mu$-tracks are shown for corsika (a) and $\nu_{atm}$ (b). All plots are normalized individually to the same number of events. Figures on the left show inclusive events. Figures on the right show exclusive TE-1 (FPGA-TE) and TE-2 (6D-TE) events. The displayed events are the same as those shown in figures 5.8 (a) and (b).

A simulated $\nu_{atm}$ of 110 GeV, with an extremely low number of hit HLC-DOMs of 2, but a fairly good number of SLC-DOMs on several strings, gives an idea of the class of events that are exclusively captured with the TE

method (figure 5.10). This event can be kept and reconstructed accurately, although the interaction vertex lies in between 2 IceCube strings, with the muon traveling parallel to the corridor between strings.

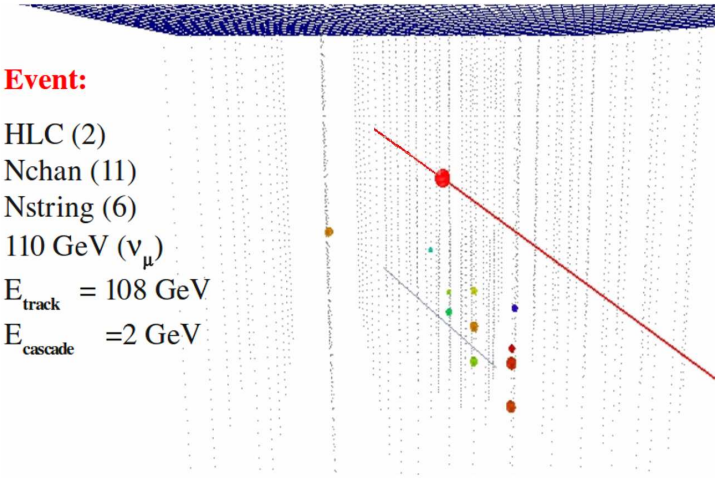


Figure 5.10: Exclusive low energy $\nu_{atm}$ event, triggered by TE-1. The grey line indicates the true MC $\mu$-track. The red line is the reconstructed TE-1 first guess direction. Both tracks are parallel and the offset is explained by the missing calculation of a proper vertex position by the TE-1. This has already been improved in TE-2 and can also be applied here, if required.

Despite the convincing performance of TE-1, the FPGA implementation has limits. The most restrictive of these is illustrated in figure 5.7. The simple binning subdivision of the sphere has 6 events (red dots) drawn within the size of a bin area (green lines). This event will be lost as TE-1 cannot take neighbouring bins into consideration. Therefore, TE-2 is changing to the healpix subdivision of the sphere. TE-2 currently exists only in software, capable of reading out adjacent bins. The histogramming stage is improved from a 2 to a 6 dimensional histogram. Studies with TE-1 indicate that the preferred bin size appears to be a fraction larger than the one chosen within the 344 simple bins. In order to allow larger bin sizes within the healpix map, the more selective multidimensional approach is needed to avoid an increase in random triggers. Figures 5.8 (a) and (b) show for the current developed TE-2 trigger an even more significant increase in the number of accepted low energy events. But at this stage of the development of the TE-2 trigger, it is not yet clear how usable these exclusive TE-2 events are for point source

searches like a solar WIMP analysis. One will reach the limit of being able to reconstruct the muon direction for these extremely dim events.

## 5.7 Data Filtering and processing

The IceCube 79 string detector trigger rate is about 2400 Hz. All triggering events are passed on to the on-line processing and filtering (PnF) farm in the IceCube laboratory at the South Pole. During the PnF filtering steps, all events undergo calibration, pulse extraction and noise cleaning. Photon arrival times and intensities within the optical sensors are calculated and then fitted with a muon track hypothesis. These track fits are used in a series of physics filters, to select further interesting physics events and to reduce the event rate. For the IceCube-79 string configuration, the PnF filter rate totaled 160 Hz, corresponding to a data volume of 70 GB per day. For the solar WIMP analysis, three physics filters are of special interest. The 'Muon-Filter', looking for up-going and horizontal muon-like events with a zenith angle greater than 70 degrees. This threshold is further reduced for high energy events. The 'LowUp-Filter', targets low-energy up-going neutrino events in general, to be used e.g. for WIMP searches and atmospheric neutrino analyses. It tries to capture up-going muons below 1 TeV. This filter is proposed to accommodate CylinderTrigger events, as discussed in section 5.6.1 that are available for the first time from the start of the full IceCube-86 string run. The third filter, the 'DeepCore-Filter', is a dedicated DeepCore filter. It selects low energy events within the DeepCore fiducial volume. The filter algorithm applies a simple veto to the cosmic ray muon background events that dominates the low energy data set by using the surrounding IceCube detector as an active veto shield.

# Chapter 6

# IceCube-80 + DeepCore-6 solar WIMP sensitivity

## 6.1 Introduction and conventions

This IceCube-80 and DeepCore-6 sensitivity study aims to update the first sensitivity study, discussed in Ref. [85], which was made for the DeepCore proposal. In the initial work, DeepCore consisted of 6 additional strings, illustrated in figure 6.1, with 40 standard IceCube DOMs with 10 meters spacing that are deployed between 2060 m and 2450 m below the ice surface. This new analysis uses the actual deployed DeepCore geometry with HQE-DOMs instead of standard DOMs and a denser spacing of only 7 m between modules (see also section 5.2 for more details). Additionally, string 36, the center string within IceCube is instrumented with several HQE-DOMs, which are deployed below the main dust layer starting at a depth of 2060 m. In this study, strings 79 and 80 were assumed to be at the positions originally planned for them. (In reality, they were deployed in 2010 as additional DeepCore strings.) The work also includes a sensitivity estimate for the IceCube 80-string detector for comparison, to evaluate the enhanced low energy reach for a potential solar WIMP signal with DeepCore. The used detector geometries are shown in figure 6.1. The AMANDA array is not considered in this analysis.

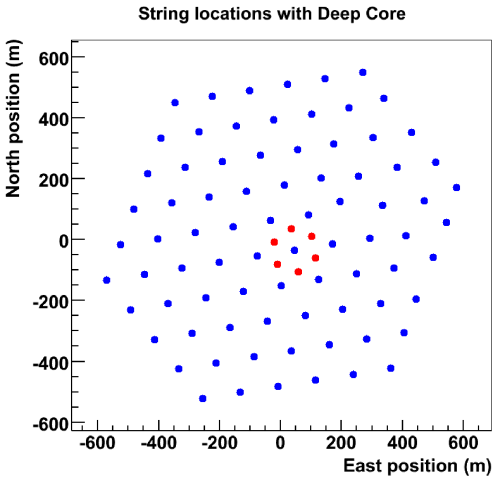


Figure 6.1: Top view of detector geometry used in sensitivity study. Standard IceCube string positions are indicated in blue and make up the reference IceCube-80 string detector. The additional DeepCore strings, as considered here, are marked in red.

## simulated datasets

This study is based on datasets generated with simulation release V02-02-09 using AHA07v2 photon tables. Datasets and their corresponding livetimes are listed in table 6.1,

### background simulations

The atmospheric muon background simulations includes apart from single muon events, two muon coincidences within the detector, as well as three muon coincidences. The atmospheric muon neutrino sample is simulated with $3 \cdot 10^5$ triggering events and a corresponding detector livetime of 180 days.

### signal simulations

WIMP signals are generated for 7 different WIMP masses with the 'hard', 'soft' and 'LKP' spectra as discussed in section 2.8. The selected masses are: 50 GeV, 100 GeV, 250 GeV, 500 GeV, 1000 GeV, 3000, GeV and 5000 GeV

Table 6.1: Background simulations, listed by dataset and livetime.

| | single-atm.$\mu$ | 2-coin.atm.$\mu$ | 3-coin.atm.$\mu$ | atm.$\nu_\mu$ |
|---|---|---|---|---|
| livetime | $\sim$ 1h | $\sim$ 4h | $\sim$ 1d | $\sim$ 180d |
| dataset | 1509 | 1511 | 1550 | 1560 |

for the 'hard' and 'soft' neutralino channels, and 300 GeV, 500 GeV, 700 GeV, 900 GeV, 1100 GeV, 1300, GeV and 1500 GeV for the 'LKP' channel. For each channel $2 \cdot 10^7$ annihilations in the Sun are simulated for the austral winter, resulting in $5 \cdot 10^4$ to $1 \cdot 10^5$ signal events triggering the detector, depending on the WIMP model.

## Trigger conditions

Three different trigger algorithms are used to trigger the detector (see section 5.5 for more details on IceCube triggers). These are the standard SMT8 trigger, the StringTrigger (5 hit DOMs within 7 adjacent DOMs on the same string within 1000 ns) and a low energy trigger, LETrigger, which is a SMT4 trigger for the fiducial DeepCore volume. The fiducial region consists of IceCube strings 26, 27, 35, 36, 37, 45 and 46 below DOM 36 and all DeepCore strings, labeled as 81, 82, 83, 84, 85 and 86 below DOM 11. All triggers run on standard hard LC, HLC, DOM launches and SLC DOM launches are not included within this analysis. The IceCube-80 string reference detector is only set to trigger on the SMT8 trigger and the StringTrigger.

## Standard filtering and track reconstruction

As discussed in section 5.7, all triggered IceCube events are subjected to online filters, which are developed in advance for each physics data year. This sensitivity study was done in parallel with the IceCube-59 string filter development, and therefore existing IceCube-59 online filters were adapted to be suitable for IceCube-86 string data. Low level filtering, L0 and L1, occurs within the standard data processing. The L0 filter eliminates noise and 'bad' hits. In the first step, hits detected by broken or 'bad' DOMs are rejected and all raw waveforms are feature extracted to identify individual pulses (the broken DOM list from the IceCube-59 detector is used). A time window (TW) cut, restricting the length of each event in time to 4500 ns is

Table 6.2: Definition of parameters used in analysis for filtering. $t_{1^{st}qu}$ and $t_{4^{th}qu}$ correspond to the first and respectively fourth quartile in time for an event. $c_M$ is the speed of light in medium. $t_{res}$ classes are defined in table 6.3. Variables indicated with † are used as input in the multivariate level $L4$.

| parameter | definition |
|---|---|
| $n_{\text{chan}}$ | number of hit DOMs |
| $n_{\text{chan,fid}}$ | number of hit DOMs in fiducial region |
| $n_{\text{chan,veto}}$ | number of hit DOMs in veto region |
| $n_{\text{str}}$ | number of hit strings |
| $n_{\text{str,veto}}$ | number of hit strings in veto region |
| $z_{\text{ext}}$ | largest extension of $\mu$ track in $z$ direction |
| separation$^{\dagger}$ | distance between cog(x, y, z,$t_{1^{st}qu}$) and cog(x, y, z,$t_{4^{th}qu}$) |
| cog x,y,z$^{\dagger}$ | center of gravity of an event in x, y, z |
| $z^{\dagger}_{\text{trav}}$ | average drift of hits in z direction, calc. from $z_{av}(t_{1^{st}qu})$ |
| $t^{\dagger}_{\text{ext}}$ | extension of time ($t_{\text{ext}} = t_{\text{last}} - t_{\text{first}}$) |
| $\phi_{\text{azi}}$ | reconstructed azimuth angle |
| $\Theta^{\dagger}_{\text{zen}}$ | reconstructed zenith angle |
| $\sigma^{\dagger}_{\text{para}}$ | paraboloid estimation of angular uncert. of llh-fit |
| rllh$^{\dagger}$ | value of loglikelihood fit divided by degrees of freedom |
| $n_{\text{dir,a(b,c,d,e)}}$ | number of hits in $t_{\text{res}}$ classes a, b, c, d and e |
| $n^{\dagger}_{\text{dir,all}}$ | $(n_{dir,a} + n_{dir,b} + n_{dir,c} + n_{dir,d} + n_{dir,e})$ |
| $l_{\text{dir,a(b,c,d,e)}}$ | largest distance along the track between $n_{dir,a(b,c,d,e)}$ |
| $l^{\dagger}_{\text{dir,all}}$ | $(l_{dir,a} + l_{dir,b} + l_{dir,c} + l_{dir,d} + l_{dir,e})$ |
| $(n^{\text{str}}_{\text{dir,a(b,c,d,e)}})^{\dagger}$ | number of strings with direct hits of classes a, b, c, d |
| $n^{str}_{dir,a+b+c}$ | $(n^{str}_{dir,a} + n^{str}_{dir,b} + n^{str}_{dir,c})$ |
| smooth$^{\dagger}_{\text{a(b,c,d)}}$ | measure of how uniformly photons are distributed along track |
| $\rho^{\dagger}_{\text{av}}$ | mean perpendicular distance from Llh-track to hit DOMs |

applied. The starting and ending point of this TW is found by maximizing the extracted charge within the defined window over the recorded event. Such a cut is only efficient for low energy signal events, like the here investigated WIMP signal events. Additionally, events are cleaned of isolated pulses.

Triggering events are mostly downgoing atmospheric muon background. A fast first guess algorithm reconstructs a probable muon track candidate to distinguish between up-and down-going muon tracks, in order to minimize the data volume for the interminable likelihood (Llh) reconstruction algorithms. First guess tracks also conduce to the Llh reconstruction algorithms as an initial track hypothesis. Within the used data processing scheme, a line-

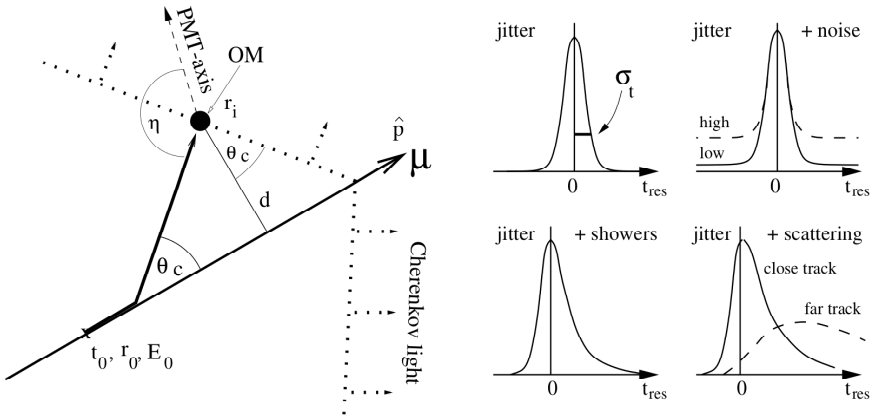


Figure 6.2: The left diagram defines coordinates for the reconstruction $(r_0, r_i, t_0, E_0, \hat{p}, d)$. The four diagrams on the right side, demonstrate the impact of different effects, like noise (top-right), hadronic showers (bottom-left) and scattering (bottom-right), and the PMT jitter distribution, defined as a Gaussian with the jitter time $\sigma_t$ (top-left) on the residual time $t_{\text{res}}$ distribution of a hit. [86]

fit first guess reconstruction is performed and used as a seed for a single iteration Llh-fit. Both muon track fit decisions are used within the adapted online filters.

### line-fit

The line-fit [87] first guess method estimates an initial track on the basis of hit times, $t_i$. It ignores specific optical properties of the medium, as well as the geometry of the Cherenkov cone, and assumes a plane wave of light with constant speed $v$ [86] traversing the detector. A $\chi^2$ variable can be defined by summing over all observed hits, $N_{\text{hit}}$,

$$\chi^2 = \sum_{i=1}^{N_{\text{hit}}} (\overrightarrow{r_i} - \overrightarrow{r} - \overrightarrow{v} \cdot t_i)^2 \quad . \tag{6.1}$$

By minimizing $\chi^2$ the fit parameters $\overrightarrow{v}$ and $\overrightarrow{r}$ are obtained. Further definitions of track variables are given in the left diagram of figure 6.2.

Table 6.3: Hit classes, defined by the time residual.

| class | time interval in ns |
|---|---|
| a | $[-15; 25]$ |
| b | $[-15; 75]$ |
| c | $[-15; 150]$ |
| d | $> -15$ |
| e | $< -15$ |

## Llh-fit

Likelihood reconstruction algorithms determine a set of unknown track parameters, $\mathbf{a}$, from a set of observed experimental values, $\mathbf{x}$, by minimizing the negative log-likelihood, $-\log \mathcal{L}(\mathbf{x}|\mathbf{a})$, defined as

$$\mathcal{L}(\mathbf{x}|\mathbf{a}) = \prod_i p(x_i|\mathbf{a}) \ . \tag{6.2}$$

$p(x_i|\mathbf{a})$ is the probability density function (pdf) of the independently measured components, $x_i$ [86]. The track parameters $\mathbf{a}$ are described by

$$\mathbf{a} = (r_0, t_0, E_0, \hat{p}) \text{ with } r_0 = (x_0, y_0, z_0, \theta, \vartheta). \tag{6.3}$$

For this analysis the patched Pandel pdf is used, which gives the probability density of observing a hit with a residual time, $t_{\text{res}} = t_{\text{hit}} - t_{\text{geo}}$, at a closest distance, $d_i$, between track and hit OM. $t_{\text{geo}}$ is the expected arrival time of a photon, calculated along the geometrical path without scattering. The patched Pandel is based on the Pandel pdf (see eq. 6.4) that takes into account scattering and absorption of photons in ice, and is parametrized as

$$p(t_{res,i}|d_i) = \frac{\tau^{-d_i}/\lambda_s \cdot t_{res,i}^{d_i/\lambda_s - 1}}{\Gamma(d_i/\lambda_s)} \cdot e^{-(t_{res,i}/\tau + c t_{res,i}/n\lambda_a + d_i/\lambda_a)} \ , \tag{6.4}$$

with the scattering time, $\tau = 557$ ns, the absorption length, $\lambda_a = 98$ m, and the scattering length, $\lambda_s = 33.3$ m [88]. In order to get the patched Pandel pdf relevant for this analysis, $p(t_{res,i}|d_i)$ is patched with a Gaussian function at time $t_0$, where the width of the Gaussian is set to match the jitter time, $\sigma_t$, of the PMTs. The influence of the PMT jitter for different observed photon arrival times is illustrated in the four diagrams on the right in figure 6.2. PMT noise is added as a constant to the patched Pandel function. The observed residual time, $t_{\text{res}}$, of DOM hits can be used to estimate the goodness of the obtained Llh track, since the distribution of

$t_{\text{res}}$ of photons emitted at a distance from the DOM is well known. The different classes of hits are summarized in table 6.3. To further improve the accuracy of the reconstructed track, the iterative fit reconstruction is used. The iterative fit performs the described minimization for $N$ first guess tracks, distributed around the initial line-fit track. Furthermore, the smallest value for $-\log \mathcal{L}(\mathbf{x}|\mathbf{a})$ is determined, which corresponds to the best likelihood fit.

### paraboloid

The paraboloid reconstruction method [89] is additionally performed, to estimate the angular uncertainty of each event. `paraboloid` fits a Gaussian paraboloid function to the likelihood function in the neighborhood of the best fit. The resulting standard deviation confidence ellipse is represented by the axes $\sigma_\phi$ and $\sigma_\Theta$. The Llh track uncertainty, $\sigma_{\text{para}}$, is calculated as $\sigma_{\text{para}} = \sqrt{\frac{\sigma_\phi^2+\sigma_\Theta^2}{2}}$. Good track fits generally result in a narrow peak of the fitted paraboloid and therefore have a small $\sigma_{\text{para}}$.

The L1 filter level in this analysis consists of adapted IceCube-59 string online filters, which are used in the 'or' condition, allowing an event to pass the L1 filter when the event fulfills only one of the three filter conditions. The Muon-filter and the LowUp-filter are upgoing muon filters, based on the above discussed first guess track fits. The LowUp-filter has an improved acceptance for low energies than the Muon-filter. The third L1 filter, the Contained-filter, selects events with a reconstructed interaction vertex inside the fiducial volume of the detector. Events passing L1 are then further reconstructed with a 32-iteration Llh-fit, a `paraboloid` fit, and an Llh-Fit that is weighed with a Bayesian prior for downgoing muon events.

## 6.2 Analysis cut levels

The analysis level cuts describe the consecutive chain of cuts that are applied to reduce the muon-background until the atmospheric neutrino level is reached. As this sensitivity study is limited by muon background simulation statistics, it was decided to cut very hard in the last cut level. This guarantees a more conservative, but also more reliable estimate of the sensitivity. Expected background rates at various cut levels are summarized in table 6.4 and the cut efficiency for background and signal at different levels is shown

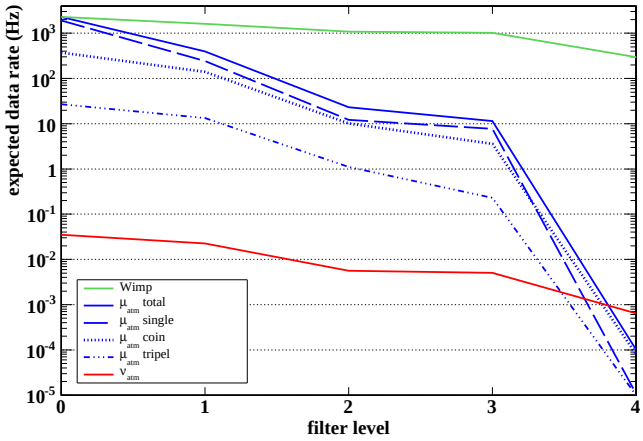


Figure 6.3: Efficiency at different filter levels for background and 1000 GeV hard $\chi$ signal. All backgrounds are scaled to the expected data rate at various cut levels, and indicated as presented in legend. The signal is scaled at trigger level, $L0$, to the expected total background rate for better illustration.

in figure 6.3 for a example signal of 1000 GeV hard.

In order to simplify the filtering process for two detector configurations and 21 different WIMP models, 14 different Neutralino models with masses ranging from 50 GeV to 5000 GeV and 7 LKP models with masses between 300 GeV to 1500 GeV, filter levels L2 and L3 are not optimized individually for each WIMP model. In contrast, the TMVA [90] based multivariate cut level L4 is optimized for three classes of models per detector configuration, which are grouped in table 6.5. Starting with L4, the three model groups are optimized separately.

Table 6.4: Expected rates at various analysis levels. Cuts are uniform till level 3. Level 4 rates can differ slightly, depending on the investigated WIMP model. Shown rates are for 1000 GeV hard for the IC80+DC6 configuration.

| cut level | total atm.$\mu$ (Hz) | single-atm.$\mu$ (Hz) | 2-coin.atm.$\mu$ (Hz) | 3-coin.atm.$\mu$ (Hz) | atm.$\nu_\mu$ (mHz) |
|---|---|---|---|---|---|
| trigger | 2303 | 1903 | 372.5 | 27.1 | 35.2 |
| level 1 | 396 | 242.9 | 140.3 | 13.3 | 22.6 |
| level 2 | 23.3 | 12.1 | 10.1 | 1.1 | 5.65 |
| level 3 | 11.5 | 7.7 | 3.6 | 0.23 | 5.04 |
| level 4 | $< 1.2 \cdot 10^{-4}$ | $1.0 \cdot 10^{-5}$ | $< 1.0 \cdot 10^{-4}$ | $< 1.0 \cdot 10^{-5}$ | 0.64 |

Table 6.5: WIMP model groups for cut optimization after $L3$. Bold are shown models, serving as the representative signal of the group within $L4$.

| group | description | WIMP models |
|---|---|---|
| I | low energy $\chi$ | hard: 50, **100** GeV |
| | | soft: 50, 100, 250 GeV |
| II | high energy $\chi$ | hard: 250, 500, **1000**, 3000, 5000 GeV |
| | | soft: 500, 1000, 3000, 5000 GeV |
| III | all LKP | 300, 500, **700**, 900 GeV |
| | | 1100, 1300, 1500 GeV |

## level L2

The L2 acceptance requirements are (variable are defined in table 6.2):

- $[86° < \Theta_{\text{zen}} < 120°]$;
- $z_{\text{trav}} > -30$ m;
- $n_{\text{str}} > 1$;

The L2 cut level selects events within a wider reconstructed zenith angle range compared to the traditionally used range. This allows for the possible reconstructed error of low energy signal events. This is especially important for the low energy $\chi$ channels, which have a rather flat reconstructed zenith angle spectrum compared to the high energy $\chi$ channels. Additionally, single string events are neglected and a cut on $z_{trav}$ is applied.

## level L3

The L3 selection imposes the requirements (variable are defined in table 6.2):

- $\rho_{av} < 100$ m;
- $z_{\text{ext}} < 400$ m;

Level 3 is devoted to further select events with horizontal and contained tracks. The purpose of the L3 cut is to remove distribution tails, dominated by background, before the multivariate selection at L4. The cuts are optimized to keep more than 95% of signal events. Within a real data analysis, these cuts would be placed slightly harder, as the data volume needs to be reduced to a smaller rate. Both parameter distributions are shown in figure 6.4 before the applied level 3 cuts.

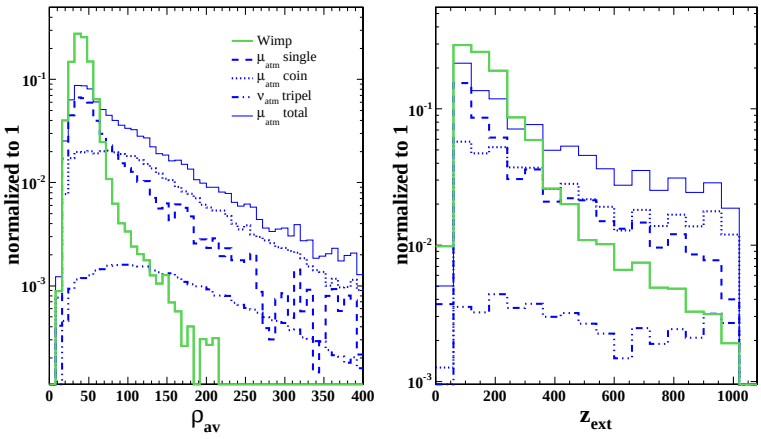


Figure 6.4: Cut variables for level 3. WIMP signal (1000 GeV hard) and different atmospheric muon backgrounds are shown as indicated in the legend. The total muon background and the signal is normalized to 1.

## level L4

The multivariate filter level, L4, consists of a combination of two different TMVA methods to separate efficiently between signal and background. Input parameters, which have low correlation, but high discrimination power between background and signal were selected. These are listed in table 6.2 and illustrated in figures 6.5 and 6.6. All investigated TMVA routines, like support vector machines (SVM), neural networks (NN) and boosted decision trees (BDT), are trained and tested on special signal and background event samples. Both samples contain events that are not used otherwise throughout the analysis and are discarded after the multivariate training and testing phase to avoid bias. The chosen background sample contains single and coincidence atm. muon events. For each signal sample defined by the combination of detector configuration and signal group, the best cut on any combination of the multivariate output parameters $Q_1$ and $Q_2$ is found through a series of test trials. Wherefore, the model rejection factor [91], MRF, is used to find the optimum cut value and TMVA methods for a fixed solar cone around the Sun (see further details on solar cone and MRF below). The fixed cone for signal group I was set to 10° and 6° for group II and III.

In this optimization process, a BDT and NN are found to result in the best cut efficiency. Final BDT score $Q_1$ and NN score $Q_2$ are shown in figure 6.7 together with the combined L4 cut parameter $Q_1 \cdot Q_2$. The L4 selection imposes the following requirements on $Q_1 \cdot Q_2$ (requirement is given for each

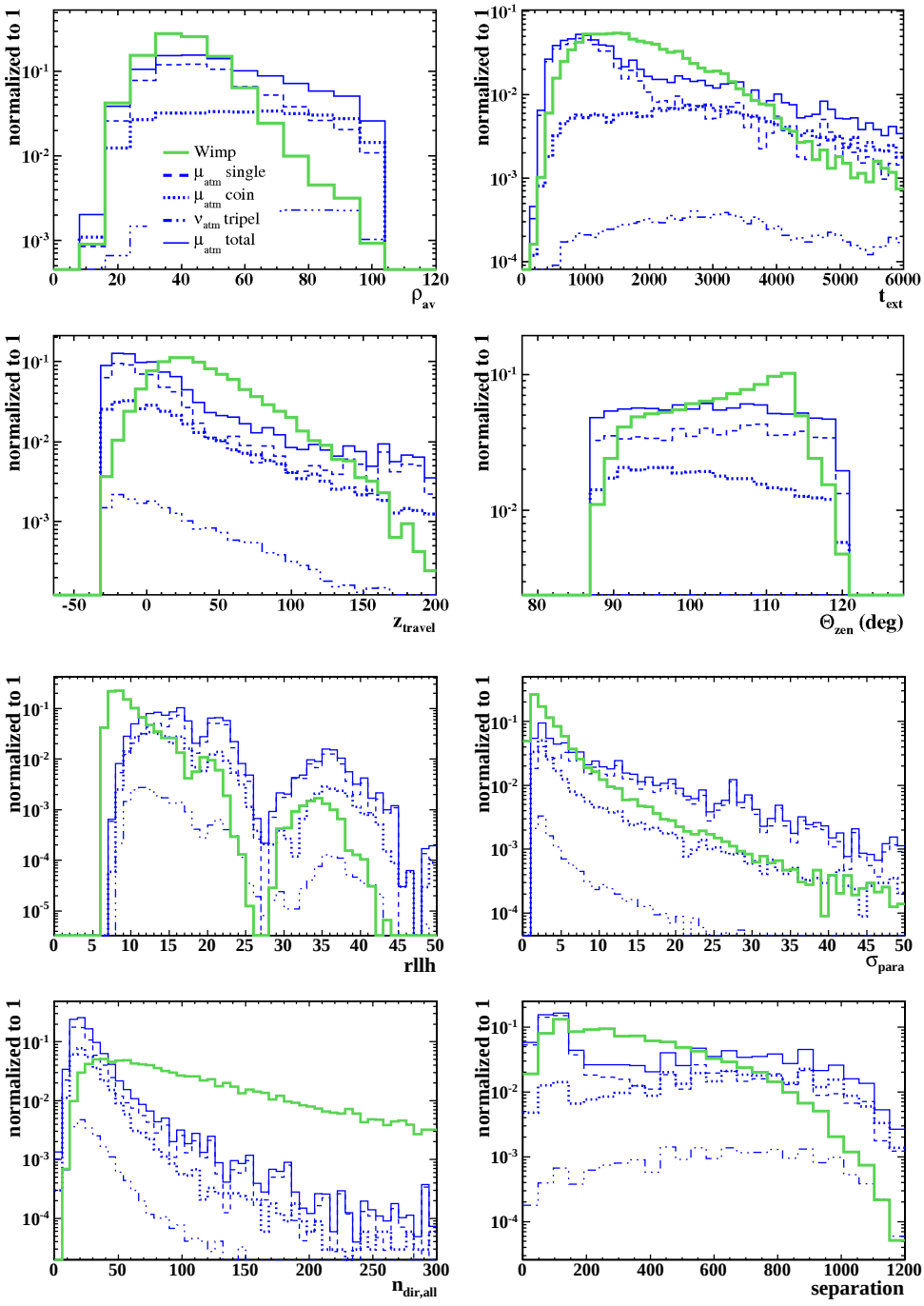


Figure 6.5: TMVA input variables. WIMP signal (1000 GeV hard) and different atmospheric muon backgrounds are shown as indicated in the legend. The total muon background and the signal is normalized to 1.

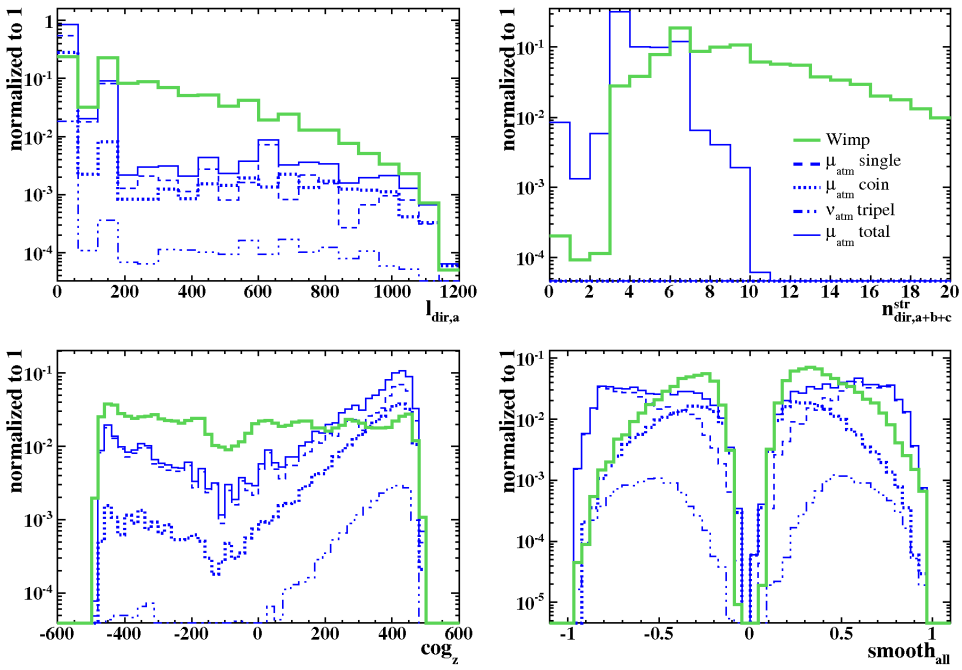


Figure 6.6: TMVA input variables. WIMP signal (1000 GeV hard) and different atmospheric muon backgrounds are shown as indicated in the legend. The total muon background and the signal is normalized to 1.

combination of detector configuration and signal group):

- $Q_1 \cdot Q_2 > 0.44$ ( $> 0.35$ IceCube-80 string) $\mapsto$ group-I;
- $Q_1 \cdot Q_2 > 0.46$ ( $> 0.35$ IceCube-80 string) $\mapsto$ group-II;
- $Q_1 \cdot Q_2 > 0.60$ ( $> 0.41$ IceCube-80 string) $\mapsto$ group-III;

As discussed earlier in this chapter, due to the limited available simulation samples, the analysis is designed with harder cuts than evidently necessary from L4 filter results. The combined L4 cut on the BDT and NN scores is succeeded by post TMVA cuts (listed in table 6.6) for the different signal groups.

## Solar cone and MRF

After L4 cuts, the $\mu_{atm}$ background reduction is $< 5.2 \cdot 10^{-8}$, which implies that surviving events in the final sample are dominated by $\nu_{atm}$ background.

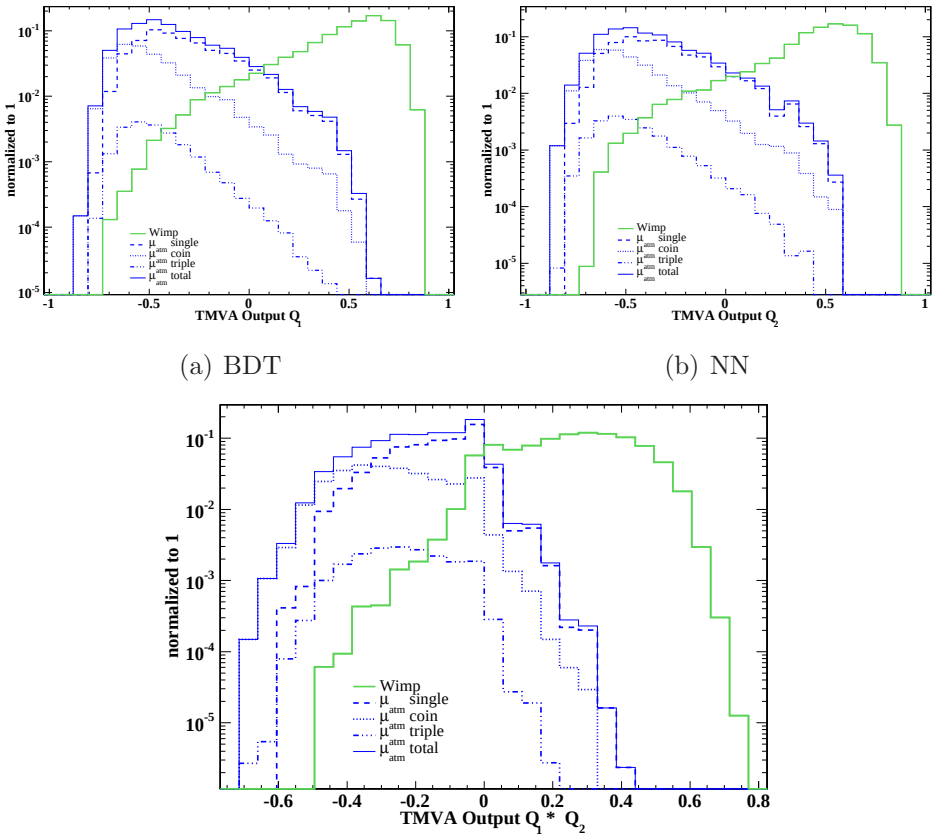


(a) BDT

(b) NN

(c) NN x BDT

Figure 6.7: NN and BDT final scores, as well as the combined cut parameter ($Q_1 \cdot Q_2$). WIMP signal (1000 GeV hard) and different atmospheric muon backgrounds are shown as indicated in the legend. The total muon background and the signal is normalized to 1.

This can also be seen in figure 6.3. The solar WIMP search is looking for an excess in neutrino events over the expected background from the direction of the Sun. Probability distributions for signal and $\nu_{atm}$ background can be constructed that are based on $\Psi$, the angle between the reconstructed Llh track and the direction of the Sun. $f_s(\Psi)$, the signal probability distribution is well known for each model from simulation. The background probability distribution, $f_{bg}(\Psi)$, is found by randomizing the azimuth angle in the final event sample, here $\nu_{atm}$ simulation. Both distributions are shown in figures 6.8 (a) and (b). The signal simulation corresponds to the 100 GeV hard $\chi$ model.

In the process of finding the optimum solar search cone, which results in the

Table 6.6: post $L4$ cuts per signal group

| group | description | WIMP models |
|---|---|---|
| I | low energy $\chi$ | $n_{\mathrm{dir,a+b+c+d}} < 180$, $l_{\mathrm{dir,a+b+c+d}} < 300$ m |
| | | $\mathrm{smooth}_{\mathrm{a+b+c+d}} > -0.6$, $n_{str} < 8$, $n_{\mathrm{str,veto}} < 3$ |
| II | high energy $\chi$ | $l_{\mathrm{dir,a+b+c+d}} > 500$ m, $n_{str} > 2$ |
| III | all LKP | $l_{\mathrm{dir,a+b+c+d}} > 500$ m, $n_{\mathrm{str}} > 2$ |

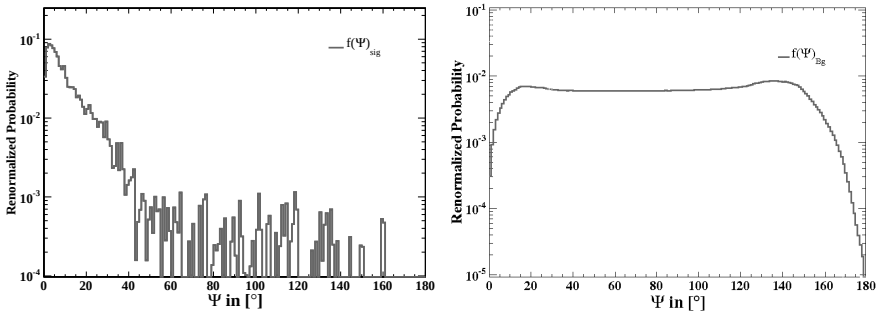


(a) pdf( sig ) (b) pdf( bg )

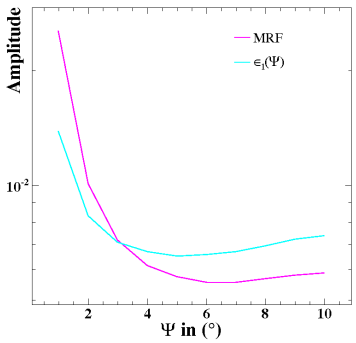


(c) MRF

Figure 6.8: Plot (a) shows the renormalized signal pdf for angle $\Psi$ for signal (100 GeV hard) and plot (b) the renormalized background pdf. Plot (c) shows for the cases of plots (a) and (b) both optimization methods to find the optimum search cone cut. In this analysis the MRF is used.

highest possible sensitivity for this study with a total livetime $t_{\mathrm{live}} = 180$ d, two different optimizations were investigated:

$$\epsilon_1(\Psi) = \frac{\sqrt{n_{\mathrm{Bg}}}}{n_s} \qquad \mathrm{MRF} = \frac{\bar{\mu}_s^{90\%}}{n_s} \tag{6.5}$$

$n_s$ and $n_{\mathrm{Bg}}$ are the number of signal and background events, respectively, in the cone. $\overline{\mu}_s^{90\%}$ is the average Feldman-Cousins 90% confidence upper limit on the expected signal [92]. $\overline{\mu}_s^{90\%}$ is used to estimate a sensitivity of an experiment, without looking at the actual data. The so called Feldman-Cousin sensitivity is determined for experiments under the assumption of a large number of hypothetical repetitions of the same experiment with an expected background $n_{\mathrm{Bg}}$ and no true observed signal ($n_s = 0$) [91]. The average upper limit is given by the sum over all hypothetically observed events $n_{\mathrm{obs}}$ in the pseudo experiments weighted by their Poisson probability of occurrence,

$$\overline{\mu}_s^{90\%}(n_{\mathrm{Bg}}) = \sum_{n_{\mathrm{obs}}=0}^{\infty} \mu_s^{90\%}(n_{\mathrm{obs}}, n_{\mathrm{Bg}}) \frac{(n_{\mathrm{Bg}})^{n_{\mathrm{obs}}}}{(n_{\mathrm{obs}})!} e^{-n_{\mathrm{Bg}}} \ . \tag{6.6}$$

The model rejection factor (MRF) is used to determine the optimized search cone, because expected limit on the neutrino-to-muon conversion rate in the absence of a signal, $\overline{\Gamma}_{\nu\to\mu}^{90\%}$, is directly proportional to the MRF. Both investigated optimization methods are shown for the example of the 100 GeV hard $\chi$ model in figure 6.8 (c) and the obtained values for $\Psi$, $\bar{\mu}_s^{90\%}$ and resulting effective volume, $V_{\mathrm{eff}}$, for each signal group are listed in table 6.7. $V_{\mathrm{eff}}$ at final analysis level for all different signal models and detector configurations is illustrated in figure 6.9.

## 6.3 Sensitivity

The total number of background events expected during one austral winter can be derived from the sum of all background rates at final filter level. This is, for example, calculated to 11820 events in the final sample for cuts corresponding to signal group II. Under the assumption of no signal, it is possible to derive the above discussed Feldman-Cousin sensitivity for the analyzed detector configurations.

The physical quantity that neutrino telescopes measure directly or set limits on, is the neutrino-to-muon conversion rate $\Gamma_{\nu\to\mu}$, given by

$$\Gamma_{\nu\to\mu} = \frac{\mu_s}{V_{\mathrm{eff}} \cdot t_{\mathrm{live}}} \ . \tag{6.7}$$

For each signal model, one can separately calculate the $V_{\mathrm{eff}}$ within the optimized solar search cone. For each $\overline{\Gamma}_{\nu\to\mu}^{90\%}$, the limit on the annihilation rate in

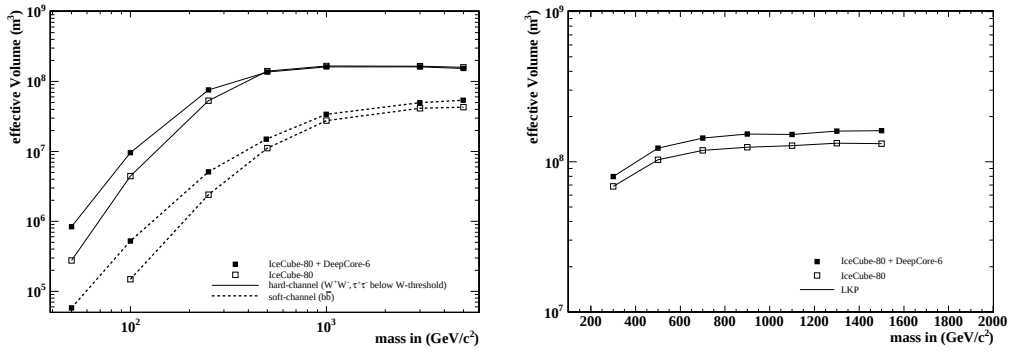


(a) neutralino (b) LKP

Figure 6.9: Effective volume at final analysis level for the case of $\chi$ DM (a) and LKP DM (b). Detector configurations and WIMP models are indicated in legend.

the core of the Sun is given by,

$$\overline{\Gamma}_A^{90\%} = (c_1(\mathrm{ch}, m_{\mathrm{DM}}))^{-1} \cdot \overline{\Gamma}_{\nu\to\mu}^{90\%} \ , \tag{6.8}$$

where $c_1(\mathrm{ch}, m_{\mathrm{DM}})$ is a conversion factor, depending on signal channel and WIMP mass. The corresponding muon flux at a plane at the detector is then derived with,

$$\Phi_\mu^{90\%}(E_\mu > E_{\mathrm{thr}}) = \frac{\overline{\Gamma}_A^{90\%}}{4\pi r_\odot^2} \cdot \int_{E_{\mathrm{thr}}}^{\infty} dE_\mu \frac{dN}{dE_\mu} = \overline{\Gamma}_A^{90\%} \cdot c_2(\mathrm{ch}, m_{\mathrm{DM}}) \ , \tag{6.9}$$

where $r_\odot$ is the distance Earth-Sun, which is 1AU, and the energy threshold for muon detection for neutrino telescopes is set to 1 GeV. $\frac{dN}{dE_\mu}$ is the differential number of muons produced at the detector location at a given energy from WIMP annihilations in the Sun and $c_2(\mathrm{ch}, m_{\mathrm{DM}})$ is another conversion factor per annihilation channel and WIMP mass. The calculation chain $\overline{\Gamma}_{\nu\to\mu}^{90\%} \to \overline{\Gamma}_A^{90\%} \to \Phi_\mu^{90\%}$ is performed using the WimpSim code described in [93, 94]. In section 2.8, it is shown that the capture rate and annihilation rate in the Sun are related in equilibrium. Also shown is that the capture rate is related to the WIMP-proton scattering cross sections $\sigma_{SI}$ and $\sigma_{SD}$. By assuming that the capture is dominated either by spin independent or spin dependent scattering, it is possible to derive sensitivities for $\sigma_{SI}$ and $\sigma_{SD}$ [58]. Sensitivities on the muon flux and $\sigma_{SD}$ at the 90% confidence level are summarized in table 6.8 and illustrated in figures 6.10 and 6.11 for the example of $\chi$ DM, and in figure 6.12 for the case of the LKP.

Table 6.7: Summary table (1). Optimum cone cut value $\Psi_{cone}$ and average Feldman-Cousins 90% confidence upper limit on the expected signal, $\bar{\mu}^{90\%}$ and $V_{eff}$ are listed per signal model, mass and detector configuration.

| $m_{\chi,LKP}$ (GeV) | model | $\Psi_{cone}$ (deg) | IceCube-80 + DeepCore-6 $\bar{\mu}^{90\%}$ | IceCube-80 + DeepCore-6 $V_{eff}$ (km$^3$) | IceCube-80 $\bar{\mu}^{90\%}$ | IceCube-80 $V_{eff}$ (km$^3$) |
|---|---|---|---|---|---|---|
| 50 | soft | 7 | 12.10 | $5.8 \cdot 10^{-5}$ | – – – – | – – – – |
| 100 | soft | 7 | 12.10 | $5.2 \cdot 10^{-4}$ | 6.71 | $1.5 \cdot 10^{-4}$ |
| 250 | soft | 7 | 12.10 | $5.1 \cdot 10^{-3}$ | 6.71 | $2.4 \cdot 10^{-3}$ |
| 500 | soft | 3 | 7.73 | $1.3 \cdot 10^{-2}$ | 7.83 | $1.2 \cdot 10^{-2}$ |
| 1000 | soft | 3 | 7.73 | $3.1 \cdot 10^{-2}$ | 7.83 | $3.0 \cdot 10^{-2}$ |
| 3000 | soft | 3 | 7.73 | $5.2 \cdot 10^{-2}$ | 7.83 | $3.5 \cdot 10^{-2}$ |
| 5000 | soft | 3 | 7.73 | $5.8 \cdot 10^{-2}$ | 7.83 | $3.8 \cdot 10^{-2}$ |
| 50 | hard | 7 | 12.10 | $8.4 \cdot 10^{-4}$ | 6.71 | $2.7 \cdot 10^{-4}$ |
| 100 | hard | 7 | 12.10 | $9.6 \cdot 10^{-3}$ | 6.71 | $4.4 \cdot 10^{-3}$ |
| 250 | hard | 3 | 7.73 | $7.6 \cdot 10^{-2}$ | 7.83 | $5.3 \cdot 10^{-2}$ |
| 500 | hard | 3 | 7.73 | $1.4 \cdot 10^{-1}$ | 7.83 | $1.4 \cdot 10^{-1}$ |
| 1000 | hard | 3 | 7.73 | $1.6 \cdot 10^{-1}$ | 7.83 | $1.7 \cdot 10^{-1}$ |
| 3000 | hard | 3 | 7.73 | $1.6 \cdot 10^{-1}$ | 7.83 | $1.6 \cdot 10^{-1}$ |
| 5000 | hard | 3 | 7.73 | $1.5 \cdot 10^{-1}$ | 7.83 | $1.6 \cdot 10^{-1}$ |
| 300 | LKP | 3 | 6.85 | $7.9 \cdot 10^{-2}$ | 6.48 | $6.9 \cdot 10^{-2}$ |
| 500 | LKP | 3 | 6.85 | $1.2 \cdot 10^{-1}$ | 6.48 | $1.0 \cdot 10^{-1}$ |
| 700 | LKP | 3 | 6.85 | $1.4 \cdot 10^{-1}$ | 6.48 | $1.2 \cdot 10^{-1}$ |
| 900 | LKP | 3 | 6.85 | $1.5 \cdot 10^{-1}$ | 6.48 | $1.3 \cdot 10^{-1}$ |
| 1100 | LKP | 3 | 6.85 | $1.5 \cdot 10^{-1}$ | 6.48 | $1.3 \cdot 10^{-1}$ |
| 1300 | LKP | 3 | 6.85 | $1.6 \cdot 10^{-1}$ | 6.48 | $1.3 \cdot 10^{-1}$ |
| 1500 | LKP | 3 | 6.85 | $1.6 \cdot 10^{-1}$ | 6.48 | $1.3 \cdot 10^{-1}$ |

## 6.4 Discussion

Figures 6.10 and 6.11 demonstrate clearly the enhanced low energy reach of the IceCube-80 string detector together with the DeepCore sub-detector, compared to the IceCube-80 string configuration only. In the case of the LKP the combined detector sensitivity is indicated, in figure 6.12, and compared to the current best limit from the IceCube-22 string configuration. The differential neutrino energy spectrum resulting from LKP annihilations is very hard. As described in chapter 2.6, the lower limit on the LKP mass is roughly 300 GeV higher than the one for $\chi$ DM candidates. Hence, DeepCore does not contribute significantly to the final sensitivity and both investigated detector configurations are comparable.

Table 6.8: Summary table (2). Final sensitivities on the muon flux and $\sigma_{SD}$ at the 90% confidence level are listed per signal model, mass and detector configuration.

| $m_{\chi,LKP}$ (GeV) | model | IceCube-80 + DeepCore-6 | | IceCube-80 | |
|---|---|---|---|---|---|
| | | $\bar{\Phi}_\mu(\mathrm{km}^{-2}\mathrm{y}^{-1})$ | $\bar{\sigma}_{SD}$ (pb) | $\bar{\Phi}_\mu(\mathrm{km}^{-2}\mathrm{y}^{-1})$ | $\bar{\sigma}_{SD}$ (pb) |
| 50 | soft | 7758.94 | $1.7 \cdot 10^{-2}$ | $----$ | $----$ |
| 100 | soft | 1892.59 | $4.7 \cdot 10^{-3}$ | 3708.57 | $9.2 \cdot 10^{-3}$ |
| 250 | soft | 381.73 | $1.6 \cdot 10^{-3}$ | 447.32 | $1.8 \cdot 10^{-3}$ |
| 500 | soft | 145.21 | $1.1 \cdot 10^{-3}$ | 159.23 | $1.2 \cdot 10^{-3}$ |
| 1000 | soft | 83.42 | $1.4 \cdot 10^{-3}$ | 89.03 | $1.5 \cdot 10^{-3}$ |
| 3000 | soft | 66.37 | $6.1 \cdot 10$ | 101.18 | $9.2 \cdot 10^{-3}$ |
| 5000 | soft | 63.44 | $1.4 \cdot 10^{-2}$ | 98.10 | $2.2 \cdot 10^{-2}$ |
| 50 | hard | 1620.12 | $1.5 \cdot 10^{-4}$ | 2722.99 | $2.6 \cdot 10^{-4}$ |
| 100 | hard | 284.10 | $6.4 \cdot 10^{-5}$ | 341.8 | $7.7 \cdot 10^{-5}$ |
| 250 | hard | 55.91 | $1.8 \cdot 10^{-5}$ | 80.33 | $2.6 \cdot 10^{-5}$ |
| 500 | hard | 48.17 | $3.4 \cdot 10^{-5}$ | 47.47 | $3.4 \cdot 10^{-5}$ |
| 1000 | hard | 50.88 | $1.2 \cdot 10^{-4}$ | 50.48 | $1.2 \cdot 10^{-4}$ |
| 3000 | hard | 51.21 | $1.5 \cdot 10^{-3}$ | 51.11 | $1.5 \cdot 10^{-3}$ |
| 5000 | hard | 52.11 | $5.3 \cdot 10^{-3}$ | 51.06 | $5.1 \cdot 10^{-3}$ |
| 300 | LKP | 50.02 | $2.2 \cdot 10^{-5}$ | 54.98 | $2.4 \cdot 10^{-5}$ |
| 500 | LKP | 43.68 | $3.4 \cdot 10^{-5}$ | 49.68 | $3.9 \cdot 10^{-5}$ |
| 700 | LKP | 42.37 | $5.6 \cdot 10^{-5}$ | 48.39 | $6.4 \cdot 10^{-5}$ |
| 900 | LKP | 43.22 | $8.8 \cdot 10^{-5}$ | 49.97 | $1.0 \cdot 10^{-4}$ |
| 1100 | LKP | 45.50 | $1.4 \cdot 10^{-4}$ | 51.23 | $1.5 \cdot 10^{-4}$ |
| 1300 | LKP | 44.28 | $1.8 \cdot 10^{-4}$ | 50.55 | $2.1 \cdot 10^{-4}$ |
| 1500 | LKP | 45.39 | $2.5 \cdot 10^{-4}$ | 52.34 | $2.9 \cdot 10^{-4}$ |

A careful comparison of the numbers quoted in table 6.8 and the curves in figures 6.10 and 6.11 shows a small deviation for the IceCube-80 + DeepCore-6 configuration at the lowest masses. The difference is summarized in table 6.9 and results from a conservative estimate in how much IceCube can improve the median angular resolution of low energy muon events and is motivated below. It is found during this study, that events passing parts of the DeepCore fiducial area and of the IceCube detector are reconstructed less accurately than events within IceCube only. As the addition of a more sensitive fiducial detector volume such as DeepCore should in principle add more information towards a possibly more accurate track reconstruction, it seems a reasonable assumption to assume a 2 degree improvement in the median angular resolution for the lowest energies. The final sensitivities are derived under

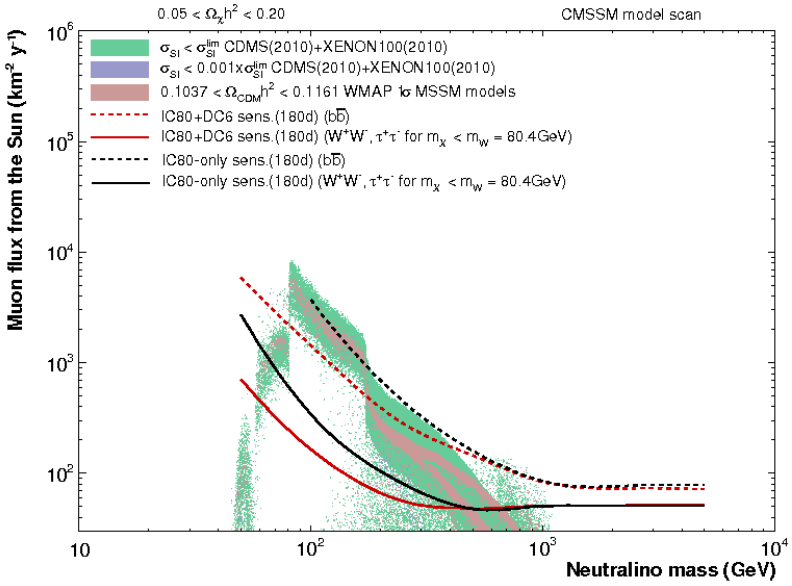


Figure 6.10: Final sensitivity on muon flux at 90% confidence level as a function of $\chi$ mass. IceCube-80 only configuration is shown in black, IceCube-80 + DeepCore-6 is shown in red. The limits for a soft WIMP annihilation spectrum are shown as dashed, while solid curves indicate the limits for a hard spectrum. The points show different SUSY models found in a cMSSM scan. Green indicates not yet excluded models; models shown in blue can be excluded by direct experiments if their sensitivity improves three orders of magnitude. In red are indicated models within the $1\sigma$ WMAP favored relic density region.

this assumption. This improvement is additionally motivated as no SLC hits are used within this study, but are available now for reconstruction. This development coincides with large efforts in finding the best possible noise hit cleaning algorithm, to separate SLC hits generated by physics from random noise hits. For the actual data analysis, further optimizations in track reconstruction techniques and data analyzing methods will be investigated and developed. The final analysis step, the search of an excess of events from the direction of the Sun within the final event selection, will also be improved from the cut and count method described here to a full likelihood method.

In summary, this study highlights the interesting prospects from a solar WIMP search with the full IceCube and DeepCore detectors for the time of only one Austral winter season. It will be possible to explore viable, non-excluded SUSY models as well Kaluza-Klein models. This work is also

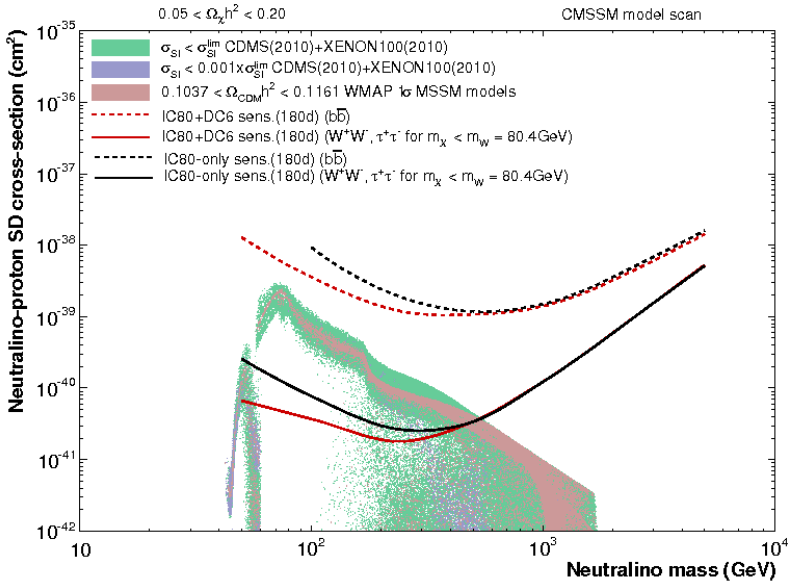


Figure 6.11: Final sensitivities on $\chi$p spin-dependent cross section at 90% confidence level as functions of $\chi$ mass. The IceCube-80 only configuration is shown in black, IceCube-80 + DeepCore-6 is shown in red. Limits on soft annihilation spectra are indicated by the dashed lines, whereas limits for hard spectra are shown as solid lines. The points show different SUSY models found in a cMSSM scan. Green indicates not yet excluded models; models shown in blue can be excluded by direct experiments if their sensitivity improves three orders of magnitude. In red are indicated models within the $1\sigma$ WMAP favored relic density region.

summarized in a shorter version within attached paper IV, where the work is also put in context with the IceCube-79 string analysis. Furthermore, the data analysis methods developed during the course of this work are applied in paper III. This paper describes a search for neutrino emission during the September 2010 Crab Nebula flare.

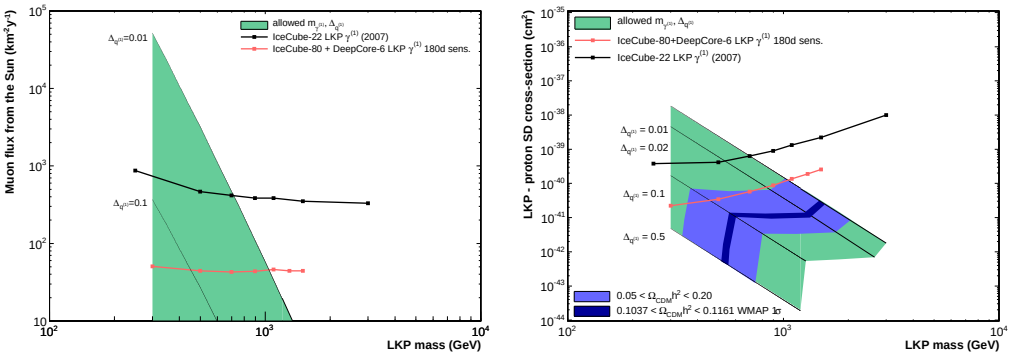


(a) muon flux (b) spin dependent cross section

Figure 6.12: (a) Limits on the muon flux from LKP annihilations in the Sun including systematic errors (squares) for the IceCube-22 string detector (black) and the final sensitivity for IceCube-80 + DeepCore-6 (red), compared to the theoretically allowed region of $m_{\gamma^{(1)}}$ and $\Delta_{q^{(1)}}$. The regions corresponding to $\Delta_{q^{(1)}} = 0.01$ and $\Delta_{q^{(1)}} = 0.1$ are marked with black lines. The region below $m_{\gamma^{(1)}} = 300$ GeV is excluded by collider experiments [16]. (b) Limits on the LKP-proton SD scattering cross-section (squares) adjusted for systematic effects for the IceCube-22 string detector (black) and the final sensitivity for IceCube-80 + DeepCore-6 (red). Theoretically predicted cross-sections are indicated by the green area [28]. The lighter blue region is allowed when considering $0.05 < \Omega_{\rm CDM}h^2 < 0.20$, and the darker blue region corresponds to the preferred $1\sigma$ WMAP (5 year) relic density $0.1037 < \Omega_{\rm CDM}h^2 < 0.1161$ [13].

Table 6.9: Muon flux and $\sigma_{SD}$ at the 90% confidence level before and after assumed average 2 degree track reconstruction improvement.

| $m_{\chi,LKP}$ (GeV) | model | orig. value | | assume 2 degree improvement | |
|---|---|---|---|---|---|
| | | $\bar{\Phi}_\mu$(km$^{-2}$y$^{-1}$) | $\bar{\sigma}_{SD}$ (pb) | $\bar{\Phi}_\mu$(km$^{-2}$y$^{-1}$) | $\bar{\sigma}_{SD}$ (pb) |
| 50 | soft | 7758.94 | $1.7 \cdot 10^{-2}$ | 5857.0 | $1.3 \cdot 10^{-2}$ |
| 100 | soft | 1892.59 | $4.7 \cdot 10^{-3}$ | 1428.8 | $3.6 \cdot 10^{-3}$ |
| 250 | soft | 381.73 | $1.6 \cdot 10^{-3}$ | 288.1 | $1.2 \cdot 10^{-3}$ |
| 50 | hard | 1620.12 | $1.5 \cdot 10^{-4}$ | 1223.0 | $1.2 \cdot 10^{-4}$ |
| 100 | hard | 284.10 | $6.4 \cdot 10^{-5}$ | 214.4 | $4.8 \cdot 10^{-5}$ |

# List of Figures


2.1 Loop violating Lorentz Invariance in 5-dimensions . . . . . 17

2.2 DAMA annual modulation . . . . . 20

2.3 FERMI positron access . . . . . 21

2.4 Simulated muon spectra from LKP, $\gamma^{(1)}$, and neutralino, $\tilde{\chi}_1^0$, annihilations . . . . . 26

2.5 Escape probability of neutrinos from the Sun . . . . . 27

2.6 Solar declination at South Pole . . . . . 27

2.7 Cartoon illustrating solar WIMP signal in IceCube . . . . . 28

3.1 Feynman diagram for $NC$ and $CC$ interaction of $\nu$ with nucleon 30

3.2 Muon range in ice and kinematic scattering angle $\Theta_{\nu-\mu}$. . . . . 32

3.3 Muon energy losses in ice . . . . . 33

3.4 Scattering and absorption length in the South Pole ice. . . . . 35

4.1 Primary CR spectrum and atm. neutrino spectrum . . . . . 38

4.2 Solar atm. $\nu$-flux and predicted number of events in IceCube . 39

5.1 3-Dim overview of the IceCube 2010 detector . . . . . 44

5.2 Schematic view of IceCube 79-string detector . . . . . 45

5.3 Average waveforms observed in PMT . . . . . 48

5.4 Illustration of Cylinder Trigger . . . . . 50

5.5 Exclusive Cylinder trigger events at trigger and filter level . . 51

5.6 Definition of quantities used in TE-1 and TE-2 . . . . . 53

5.7 Flow chart diagram illustrates the TE-1 algorithm . . . . . 54

5.8 Accumulative trigger distributions per muon energy for signal and background, including the TE. . . . . 55

5.9 Space angle distributions of true MC $\mu$-tracks compared with reconstructed $\mu$-tracks for TE events. . . . . 56

5.10 Example of an exclusive low energy $\nu_{atm}$ event, triggered by TE. 57

6.1 Top view of detector geometry used in sensitivity study . . . . 60

6.2 Reconstruction variables and PMT jitter influences . . . . . 63

6.3 Cut efficiency plot . . . . . 66

6.4 cut variables for level 3 . . . . . 68

6.5 TMVA input variables . . . . . 69

6.6 TMVA input variables . . . . . 70

6.7 NN and BDT final scores . . . . . 71

6.8 Signal and background pdf's and MRF optimization . . . . . 72

6.9 Final effective volume plots . . . . . 74

6.10 Final sensitivity on muon flux . . . . . 77

6.11 Final sensitivity on spin-dependent cross section . . . . . 78

6.12 Final sensitivity on muon flux and spin-dependent cross section for LKP . . . . . 79

# Bibliography


[1] R. et al Abbasi. Limits on a muon flux from neutralino annihilations in the sun with the icecube 22-string detector. *Phys. Rev. Lett.*, 102(20):201302, May 2009.

[2] S. Perlmutter et al. Measurements of $\Omega$ and $\Lambda$ from 42 High-Redshift Supernovae. *The Astrophysical Journal*, 517(2):565, 1999.

[3] G. Bertone, D. Hooper, and J. Silk. Particle dark matter: evidence, candidates and constraints. *Physics Reports*, 405(5-6):279–390, January 2005.

[4] David L Wiltshire. Cosmic clocks, cosmic variance and cosmic averages. *New Journal of Physics*, 9(10):377, 2007.

[5] David L. Wiltshire. Exact solution to the Averaging Problem in Cosmology. *Phys. Rev. Lett.*, 99(25):251101, Dec 2007.

[6] D. J. Fixsen et al. The cosmic microwave background spectrum from the full cobe firas data set. *The Astrophysical Journal*, 473(2):576, 1996.

[7] C. Giunti and Ch. W. Kim. *Fundamentals of Neutrino Physice and Astrophysics*. Oxford University Press, 2007.

[8] F. Zwicky. Die rotverschiebung von extragalaktischen Nebeln. *F. Helvetica Physica Acta*, 6(110), 1933.

[9] V. C. Rubin and W. K. Ford, Jr. Rotation of the andromeda nebula from a spectroscopic survey of emission regions. *The Astrophysical Journal*, 159:379, February 1970.

[10] M. Milgrom. A modification of the newtonian dynamics as a possible alternative to the hidden mass hypothesis. *The Astrophysical Journal*, 270:365–370, July 1983.

[11] Douglas Clowe, Maruša Bradač, Anthony H. Gonzalez, Maxim Markevitch, Scott W. Randall, Christine Jones, and Dennis Zaritsky. A direct empirical proof of the existence of dark matter. *The Astrophysical Journal Letters*, 648(2):L109, 2006.

[12] A Refregier. Weak gravitational lensing by large-scale structure. *ANNUAL REVIEW OF ASTRONOMY AND ASTROPHYSICS*, 41:645–668, 2003.

[13] Max et al. Tegmark. Cosmological constraints from the sdss luminous red galaxies. *Phys. Rev. D*, 74(12):123507, Dec 2006.

[14] C. J. Copi et al. Big-bang Nucleo-synthesis and the Baryon Density of the Universe. *Science*, 267(365), 1995.

[15] Piero Madau et al. Dark matter subhalos and the Dwarf Satellites of the milky way. *The Astrophysical Journal*, 679(2):1260, 2008.

[16] J. F. Oliver, J. Papavassiliou, and A. Santamaria. Universal extra dimensions and $z[over \rightarrow ]bb[over]$. *Phys. Rev. D*, 67(5):056002, Mar 2003.

[17] Howard E. Haber and Gordon L. Kane. The Search for Supersymmetry: Probing Physics Beyond the Standard Model. *Phys. Rept.*, 117:75–263, 1985.

[18] Toby Falk, Keith A. Olive, and Mark Srednicki. Heavy sneutrinos as dark matter. *Physics Letters B*, 339(3):248 – 251, 1994.

[19] P Gondolo, J Edsjö, P Ullio, L Bergström, M Schelke, and E A Baltz. Darksusy: computing supersymmetric dark matter properties numerically. *Journal of Cosmology and Astroparticle Physics*, 2004(07):008, 2004.

[20] Th. Kaluza. *Sitzungsber. Preuss. Akademische Wissenschaften Berlin Math. Phys.*, 966(K1), 1921.

[21] O. Klein. *Z. Phys.*, 895(37), 1926.

[22] Thomas Appelquist, Hsin-Chia Cheng, and Bogdan A. Dobrescu. Bounds on universal extra dimensions. *Phys. Rev. D*, 64(3):035002, Jun 2001.

[23] Edward W. Kolb and Richard Slansky. Dimensional reduction in the early universe: Where have the massive particles gone? *Physics Letters B*, 135(5-6):378 – 382, 1984.

[24] Keith R. Dienes, Emilian Dudas, and Tony Gherghetta. Grand unification at intermediate mass scales through extra dimensions. *Nuclear Physics B*, 537(1-3):47 – 108, 1999.

[25] Graham D. Kribs. Phenomenology of extra dimensions. 2006.

[26] Hsin-Chia Cheng, Konstantin T. Matchev, and Martin Schmaltz. Radiative corrections to kaluza-klein masses. *Phys. Rev. D*, 66(3):036005, Aug 2002.

[27] Géraldine Servant and Tim M. P. Tait. Is the lightest kaluza-klein particle a viable dark matter candidate? *Nuclear Physics B*, 650(1-2):391 – 419, 2003.

[28] Sebastian Arrenberg, Laura Baudis, Kyoungchul Kong, Konstantin T. Matchev, and Jonghee Yoo. Kaluza-klein dark matter: Direct detection vis-a-vis cern lhc. *Phys. Rev. D*, 78(5):056002, Sep 2008.

[29] Hsin-Chia Cheng, Jonathan L. Feng, and Konstantin T. Matchev. Kaluza-klein dark matter. *Phys. Rev. Lett.*, 89(21):211301, Oct 2002.

[30] Dan Hooper and Graham D. Kribs. Probing kaluza-klein dark matter with neutrino telescopes. *Phys. Rev. D*, 67(5):055003, Mar 2003.

[31] R. Bernabei et al. Search for WIMP annual modulation signature: Results from DAMA / NaI-3 and DAMA / NaI-4 and the global combined analysis. *Phys. Lett.*, B480:23–31, 2000.

[32] R. et al Bernabei. First results from dama/libra and the combined results with dama/nai. *The European Physical Journal C - Particles and Fields*, 56:333–355, 2008. 10.1140/epjc/s10052-008-0662-y.

[33] E. Aprile et al. The XENON dark matter search: Status of XENON10. *J. Phys. Conf. Ser.*, 39:107–110, 2006.

[34] Elena Aprile. The XENON dark matter project: Status of the XENON100 phase. *AIP Conf. Proc.*, 1166:205–211, 2009.

[35] G. J. Alner et al. Status of the ZEPLIN II experiment. *New Astron. Rev.*, 49:259–263, 2005.

[36] D. S. et al Akerib. New results from the cryogenic dark matter search experiment. *Phys. Rev. D*, 68(8):082002, Oct 2003.

[37] R. Lemrani. Search for dark matter with EDELWEISS: Status and future. *Phys. Atom. Nucl.*, 69:1967–1969, 2006.

[38] W. J. Bolte et al. A bubble chamber for dark matter detection (the COUPP project status). *J. Phys. Conf. Ser.*, 39:126–128, 2006.

[39] U. Wichoski et al. Status and results of the PICASSO experiment. *Nucl. Phys. Proc. Suppl.*, 173:121–124, 2007.

[40] B. Ahmed et al. The NAIAD experiment for WIMP searches at Boulby mine and recent results. *Astropart. Phys.*, 19:691–702, 2003.

[41] A. A. et al Abdo. Measurement of the cosmic ray $e^+ + e^-$ spectrum from 20 gev to 1 tev with the fermi large area telescope. *Phys. Rev. Lett.*, 102(18):181101, May 2009.

[42] Lars Bergström, Joakim Edsjö, and Gabrijela Zaharijas. Dark matter interpretation of recent electron and positron data. *Phys. Rev. Lett.*, 103(3):031103, Jul 2009.

[43] V. A. Balkanov et al. The lake baikal neutrino experiment. *Nuclear Physics B - Proceedings Supplements*, 87(1-3):405 – 407, 2000. Proceedings of the Sixth International Workshop on Topics in Astroparticle and Underground Physics.

[44] Y. Fukuda. Status of solar neutrino observation at Super- Kamiokande. *Nucl. Instrum. Meth.*, A503:114–117, 2003.

[45] M. Spurio and for the ANTARES collaboration. ANTARES neutrino telescope: status, first results and sensitivity for the diffuse neutrino flux. *Int. J. Mod. Phys.*, D18:1615–1619, 2009.

[46] E. Andres et al. The AMANDA neutrino telescope: Principle of operation and first results. *Astropart. Phys.*, 13:1–20, 2000.

[47] E. Resconi and for the IceCube Collaboration. Status and prospects of the IceCube neutrino telescope. *Nucl. Instrum. Meth.*, A602:7–13, 2009.

[48] Jennifer E. Carson. GLAST: physics goals and instrument status. *J. Phys. Conf. Ser.*, 60:115–118, 2007.

[49] J. A. Hinton. The status of the HESS project. *New Astron. Rev.*, 48:331–337, 2004.

[50] T. C. Weekes et al. VERITAS: the Very Energetic Radiation Imaging Telescope Array System. *Astropart. Phys.*, 17:221–243, 2002.

[51] G. Sinnis. Milagro: A low energy threshold extensive air shower array. *Nucl. Phys. Proc. Suppl.*, 43:141–144, 1995.

[52] Manel Martinez. Towards the ground-based gamma-ray observatory CTA. *AIP Conf. Proc.*, 1085:824–829, 2009.

[53] P. Picozza et al. PAMELA - A Payload for Antimatter Matter Exploration and Light-nuclei Astrophysics. *Astropart. Phys.*, 27:296–315, 2007.

[54] F. Barao. AMS: Alpha Magnetic Spectrometer on the International Space Station. *Nucl. Instrum. Meth.*, A535:134–138, 2004.

[55] Markus Ahlers, Philipp Mertsch, and Subir Sarkar. Cosmic ray acceleration in supernova remnants and the fermi/pamela data. *Phys. Rev. D*, 80(12):123017, Dec 2009.

[56] Gerard Jungman, Marc Kamionkowski, and Kim Griest. Supersymmetric dark matter. *Physics Reports*, 267(5-6):195 – 373, 1996.

[57] personal correspondence with J. Edsjö. (publication in preparation).

[58] G. Wikström and J. Edsjö. Limits on the wimp-nucleon scattering cross-section from neutrino telescopes. *Journal of Cosmology and Astroparticle Physics*, 2009(04):009, 2009.

[59] Nuclear and Particle Physics. *Review of Particle Physics. Journal of Physics,*, G33(445-471), 2006.

[60] R. Gandhi, M. H. Quigg, C. Reno, and I. Sarccvic. Ultrahigh-energy neutrino interactions. *Astroparticle-Physics*, 5(81-110), 1996.

[61] JG Learned and K Mannheim. High-energy neutrino astrophysics. *ANNUAL REVIEW OF NUCLEAR AND PARTICLE SCIENCE*, 50:679–749, 2000.

[62] C.H. Wiesbusch. The detection of faint light in deep underwater neutrino telescopes. *Ph.D Thesis*, Univ. of Aachen, 1995.

[63] P. Miocinovic. Muon energy reconstruction in the amanda. *Ph.D Thesis*, Univ. of California, Berkeley, 2001.

[64] Dmitry Chirkin and Wolfgang Rhode. Muon Monte Carlo: A high-precision tool for muon propagation through matter. 2004.

[65] D. N. Perkins. *Introduction to High Energy Physics.*, volume 4th. edition. Cambridge Univ. Press, 2000.

[66] W. R. Leo. *Techniques for Nuclear and Particle Physics Experiments: How-to Approach.*, volume Germany. Springer Verlag, 1994.

[67] M et al Ackermann. Optical properties of deep glacial ice at the south pole. *JOURNAL OF GEOPHYSICAL RESEARCH*, 111(D13203), 2006.

[68] Pingyu Liu. A new phase function approximating to mie scattering for radiative transport equations. *Physics in Medicine and Biology*, 39(6):1025, 1994.

[69] SPICEMIE DIMA. Study of south pole ice transparency with icecube flashers. *internal review*, update.

[70] William F. Hanlon. The energy spectrum of ultra high energy cosmic rays measured by the high resolution fly's eye observatory in stereoscopic mode, 2008.

[71] Paolo Lipari. Lepton spectra in the earth's atmosphere. *Astroparticle Physics*, 1(2):195 – 227, 1993.

[72] R. et al Abbasi. Measurement of the atmospheric neutrino energy spectrum from 100 gev to 400 tev with icecube. *Phys. Rev. D*, 83(1):012001, Jan 2011.

[73] T. K. Gaisser and M. Honda. Flux of atmospheric neutrinos. *Annual Review of Nuclear and Particle Science*, 52(1):153–199, 2002.

[74] Rikard Enberg, Mary Hall Reno, and Ina Sarcevic. Prompt neutrino fluxes from atmospheric charm. *Phys. Rev.*, D78:043005, 2008.

[75] G. Ingelman and M. Thunman. High energy neutrino production by cosmic ray interactions in the sun. *Phys. Rev. D*, 54(7):4385–4392, Oct 1996.

[76] G. L. Fogli, E. Lisi, A. Mirizzi, D. Montanino, and P. D. Serpico. Oscillations of solar atmosphere neutrinos. *Phys. Rev. D*, 74(9):093004, Nov 2006.

[77] Thomas K. Gaisser, Francis Halzen, and Todor Stanev. Particle astrophysics with high energy neutrinos. *Physics Reports*, 258(3):173 – 236, 1995.

[78] Kenneth Greisen. End to the cosmic-ray spectrum? *Phys. Rev. Lett.*, 16(748 - 750), 1966.

[79] A. Achterberg et al. First year performance of the icecube neutrino telescope. *Astroparticle Physics*, 26(3):155 – 173, 2006.

[80] et al Bramall, N. E. A deep high-resolution optical log of dust, ash, and stratigraphy in south pole glacial ice. *Geophys. Res. Lett.*, 32(21), 2005.

[81] The IceCube Collaboration (Ahrens et al). Icecube project preliminary design document. *http://icecube.wisc.edu*.

[82] R. Abbasi et al. The icecube data acquisition system: Signal capture, digitization, and timestamping. *Nuclear Instruments and Methods in Physics Research Section A: Accelerators, Spectrometers, Detectors and Associated Equipment*, 601(3):294 – 316, 2009.

[83] Stokstad R.G., Lowder D.M., Ludvig J., Nygren D., and Przybylski G. *LBNL-43200*, 1998.

[84] R. Abbasi et al. Calibration and characterization of the icecube photomultiplier tube. *Nuclear Instruments and Methods in Physics Research Section A: Accelerators, Spectrometers, Detectors and Associated Equipment*, 618(1-3):139 – 152, 2010.

[85] Wikström G. A serach for solar dark matter with the icecube neutrino telescope. *thesis*, ISBN 978-91-7155-881-7.

[86] The AMANDA Collaboration. Muon track reconstruction and data selection techniques in amanda. astro-ph/0407044v1, 2. July 2004.

[87] V. J. Stenger. Track fitting for dumand-ii octagon array, external report. *HDC-1-90 Unive. of Hawai'i*, 1990.

[88] D. Pandel. Bestimmung von wasser und detector parametern und rekonstruktion von myonen bis 100 tev mit dem baikal-neutrinoteleskop nt-72. *thesis*, Humboldt Univ. zu Berlin, 1996.

[89] The Gulliver and Lilliput projects. Estimating the angular resolution of tracks in neutrino telescopes based on a likelihood analysis. *Astroparticle Physics*, 25(220-225), April 2006.

[90] Andreas Hoecker, Peter Speckmayer, Joerg Stelzer, Jan Therhaag, Eckhard von Toerne, and Helge Voss. TMVA: Toolkit for Multivariate Data Analysis. *PoS*, ACAT:040, 2007.

[91] Gary C. Hill and Katherine Rawlins. Unbiased cut selection for optimal upper limits in neutrino detectors: the model rejection potential technique. *Astroparticle Physics*, 19(3):393 – 402, 2003.

[92] Gary J. Feldman and Robert D. Cousins. Unified approach to the classical statistical analysis of small signals. *Phys. Rev. D*, 57(7):3873–3889, Apr 1998.

[93] Mattias Blennow, Joakim Edsjö, and Tommy Ohlsson. Neutrinos from wimp annihilations obtained using a full three-flavor monte carlo approach. *Journal of Cosmology and Astroparticle Physics*, 2008(01):021, 2008.

[94] J. Edsjö. Wimpsim neutrino monte carlo. *http://www.physto.se/∼edsjo/wimpsim/*.